2 The 2022 Hunga plume – first month post-eruption

Lead authors Elizabeth Asher
Bernard Legras

Co-authors Marie Boichu
Julia Bruckert
Aurélien Podglajen
Ghassan Taha

Contributing authors Alexandre Baron
Simran Chopra
Stéphanie Evan
Neil Hindley
Ákos Horváth
Ali Hoshyaripour
Michelle L. Santee
Paul Walter
Pengfei Yu
Yunqian Zhu

Cite this as:

Asher, E., B. Legras et al. (2025): The 2022 Hunga plume – first month post-eruption. In APARC, 2025: The Hunga Eruption Atmospheric Impacts Report [Yunqian Zhu, Graham Mann, Paul A. Newman, William Randel (Eds.)]. APARC Report No. 11, WCRP Report No. 10/2025, DOI: 10.34734/FZJ-2025-05239, available at `https://aparc-climate.org/publications/aparc-report-no-11/`.

Key points

- A very explosive eruption (minutes to hours)
  - The plume rose rapidly through the atmosphere, overshooting to approximately 57 km altitude within the first half hour of the eruption, which occurred at approximately 4:00 UTC 15 January, 2022. The initial conditions that might explain such a high altitude are a mass proportion of 90% steam water based on simulations of the plume but this remains an open research question.
  - An unprecedented number of lightning flashes (>300,000) and lightning rate (>2,600 flashes per minute) were detected in the stratosphere over a 2-h period during the eruption, forming several rings up to a radius of 140 km.
  - Large-amplitude gravity and Lamb waves were generated by the Hunga eruption. The main Lamb waves were observed circling the globe at least four times and put this eruption in the same class as the Krakatau eruption of 1883.
- Injection of water vapour and minor components (presumably minutes; first observations within hours)
  - A remarkable feature of the Hunga eruption was the massive injection of water. The initial injection of water vapour is uncertain but is estimated to be thousands of Tg. Approximately 150 Tg of water vapour remained in the stratosphere after one day, representing an almost instantaneous increase of approximately 10% of the total mass of water in the stratosphere, which was very localised for the first weeks. The atmosphere was saturated up to at least 35 km in the immediate aftermath. These extraordinary circumstances were hypothesised but never before observed.
  - The eruption injected very minor amounts of halogens into the stratosphere and volcanic lightning, discussed above, produced nitrogen oxides (NO_x) that played a role in subsequent chemistry. The injection of halites from seawater salt remains an open research question.
- Dispersion (presumably minutes to months; first observations within hours)
  - The initial umbrella cloud dissipated entirely within 15 hours of forming, probably washed out by precipitation of ice and water, entraining the ash. The remaining plume divided into several components shortly after the eruption, with the bulk located between 24 and 32 km altitude, and with some more minor components above and below this. During the first 10 days, the main part of the plume descended as much as 4 km due to the fast cooling produced by water infrared emission, with moister parts experiencing faster descents. This cooling might also be responsible for the rapid dispersion across the equator during the first week. After two weeks (by the beginning of February and a few months thereafter), the main persistent aerosol plume stayed mostly confined to the Southern Hemisphere.
- Fast conversion to sulfates (days instead of weeks)
  - The fast conversion of SO_2 into sulfate occurred within days instead of weeks, as is usually the case in the stratosphere, due to an abundance of water vapour producing OH that accelerated the conversion. SO_2 in the moistest parts of the plume was converted faster, and the formation of the sulfate aerosol appeared complete within approximately three weeks. Except for the first two days after the eruption, satellite retrievals indicate spherical non-depolarising and non-absorbing particles and suggest a main plume composed of sulfates. The total amount of emitted SO_2 was moderate (estimated between 0.45 Tg and 1.0 Tg). The smaller SO_2 estimate (0.45 Tg) is in line with the estimated mass of the aerosol burden, based on remote sensing and in situ measurements.
- Aerosol microphysical properties (first observations within one day)
  - A consequence of the fast conversion to sulfates was fast nucleation of sulfuric acid particles, and when combined with the narrow geographic dispersion, fast growth in aerosol radius due to coagulation, reaching 0.4 μm in the main plume in a couple of weeks, instead of in four months as recorded after Pinatubo. This large particle size scatters light efficiently and produced a high AOD in the plume. After one week, water vapour enhancements had a small effect on the percent weight of sulfuric acid in the aerosol and particle radius.

Contents

Preamble

This chapter is devoted to the formation of the stratospheric plume and the sequence of events during the first month after the Hunga eruption, in particular the long-range wave propagation, the dispersion of the plume and the formation of sulfate aerosols. Section 2.1 describes the sequence of atmospheric events during the eruption and the first hours thereafter. Section 2.2 describes the waves that were generated and their long-range propagation around the Earth. Section 2.3 describes the exceptional injection of water vapour in the stratosphere. Section 2.4 describes the initial vertical and horizontal structure of the plume, its initial descent due to radiative cooling and its dispersion during the first month. Section 2.5 describes the unusually fast formation of sulfate aerosols in the plume. Section 2.6 describes the microphysical and optical properties of the aerosols. Section 2.7 describes the injection of other compounds, in particular halogens and ash. Section 2.8 discusses the sources of uncertainties and Section 2.9 fosters the value of systematic observations during such abrupt and intense events.

2.1 Initial eruption sequence

The climactic eruption of the Hunga Volcano occurred on 15 January 2022. A complex eruption sequence was detected by several methods and instruments between 04:00 and 05:00 UTC and a final eruption detected at around 08:30 to 08:40 UTC. The timing of the eruptions was initially derived from satellite observations of the plume development (Carr et al., 2022). However, the Hunga eruption also triggered different types of atmospheric waves (more details in Section 2.2) and produced both seismic and meteorological tsunamis. Backward ray-tracing of these waves helps constrain the precise timing of the eruption sequence. There were at least 4–5 constituent eruptive pulses during the main climactic eruption sequence. A summary of individual eruptive events of the main eruption identified from various observations is given in Table 2.1. Prior to the climactic eruption, the Hunga Volcano erupted intermittently between 19 December 2021 and 13–14 January 2022, with plume heights reaching between 15 and 18 km and producing ice-rich plumes (Gupta et al., 2022).

According to geostationary satellite observations, the plume appeared at about 04:10 UTC (Gupta et al., 2022) and ascended rapidly, reaching 25 km within 15 min and 40 km within 25 min (Proud et al., 2022). It formed an upper umbrella layer at about 34 km altitude (Figures 2.1a and 2.1b taken from Carr et al., 2022; Gupta et al., 2022; Proud et al., 2022) and a lower umbrella layer near 20 km (Proud et al., 2022). In-depth analysis of both visible and infrared satellite imagery, our own in Legras (2025) and that of Prata et al. (2025), undermine a claim that the plume was first observed at 02:57 UTC (Van Eaton et al., 2023). About half an hour after the start of the eruption (by 04:36 UTC), an overshooting dome formed, extending from 34 km up to at least 57 km (Figures 2.1a and b, Carr et al., 2022; Proud et al., 2022) with some small tendrils reaching 58 km. A plume injection at such altitudes is unprecedented in the satellite era. The corresponding volume injection rate into the umbrella exceeded 330 $km^3\ s^{-1}$ (Van Eaton et al., 2023; Mastin et al., 2024; Prata et al., 2025).

The overshooting top dropped to about 35 km over the next 10 min (Van Eaton et al., 2023). During the eruption, the umbrella cloud expanded horizontally with the radius increasing from 20 to 80 km within 20 min (Carr et al., 2022), and further increasing to a 200–250 km within 50 min (Gupta et al., 2022; Van Eaton et al., 2023). At 04:57 UTC, Himawari-8 images show a decrease in the expansion rate of the umbrella, which suggests a lower eruption rate overall or a total collapse of the eruption column (Proud et al., 2022; Jarvis et al., 2024).

During its 15 January eruption, Hunga was the dominant lightning source on Earth for at least the first hour of the event and impulsively charged the direct current global electric circuit twice (Bór et al., 2023). Lightning networks recorded up to 2615 flashes per minute in a combined dataset of the Global Lightning Detection Network (GLD360), the Earth Networks Total Lightning Location Network (ENTLN), and the World Wide Lightning Location Network (WWLLN, Van Eaton et al., 2023). There were 5000 strokes per minute detected from the GLD360 network alone (Bór et al., 2023) at its peak intensity at about 05:00 UTC. An unprecedented number of more than 3×10^5 flashes over a 2-h period was counted during the eruption, which decreased after 04:53 (Jarvis et al., 2024). The lightning appeared in a ring structure with the largest ring up to 140 km radius and at least four distinct lightning rings from 04:16–05:51 UTC, followed by a ring from 08:38–08:48 UTC with lightning pulses that persisted until 15:15 UTC (Van Eaton et al., 2023). The position of the initial rings are co-located with the phase front of outward-propagating gravity waves (GW) observed in stereoscopic cloud heights from Geostationary Operational Environment Satellite (GOES)-17 and Himawari-8. Lightning was observed between

Table 2.1: *Timing of the eruption events derived from a variety of observations and simulations.*

Timing in UTC	Method	Publication
04:08, 04:20, 04:28, 04:48, 04:55	Variations in ionospheric total electron content	Astafyeva et al. (2022)
~04:00 07:56, 08:06, 08:26, 08:36, 08:46 (final pulse)	Visible satellite channel Divergence in stereo plume-top motion vectors (1 min resolution)	Carr et al. (2022)
~04:00; ~08:40	Satellite brightness temperature (10 min resolution)	Gupta et al. (2022)
04:00–07:11 (main plume), 07:46–09:38 (2nd phase), 09:40–11:03, 12:11–13:07, (additional eruption activity)	Processed visible and infrared satellite channels, lightning detection from satellite and ground-based networks	Van Eaton et al. (2023)
04:07, 04:15, 04:22, 04:29 (main pulse), 08:40–08:45 (final pulse)	Pago Pago surface pressure, Lamb wave formation in satellite images	Horváth et al. (2024)
Complex timing of eruption events between 04:00 and 04:30; final major eruption at ~08:31	Infrasound and hydroacoustic stations. Seismic detection.	Matoza et al. (2022) Vergoz et al. (2022) Donner et al. (2023)
04:16	Seismic detection.	Poli and Shapiro (2022)
Pulses of emissions around 04:14, 04:53, 08:27	Stratospheric balloon observations of infrasound waves	Podglajen et al. (2022)
04:06, 04:18, 04:56	Tsunami simulations	Purkis et al. (2023)
Eruption peak at ~04:28	Peak of Lamb wave pulse in surface pressure stations	Wright et al. (2022)

20 and 30 km (Van Eaton et al., 2023). As lightning intensifies within mixed-phase clouds, these observations of high-altitude lightning suggest the eruption sustained for several hours an abundance of liquid water between 20 and 30 km altitude (Van Eaton et al., 2023).

The submarine nature of the eruption made the composition of the plume very unusual with respect to other recent documented eruptions. The minimum volume of tephra estimated from ocean-discoloration was about $1.8\,km^3 \pm 0.4\,km^3$, which is on the order of only ~12% of the caldera volume change (Kelly et al., 2024). Thus, the majority of the erupted material remained under the ocean surface and deposited on the seafloor by density currents (Clare et al., 2023; Seabrook et al., 2023), which resulted in an ash-poor plume compared to eruptions of similar magnitude. In contrast, a huge amount of ocean water was turned into steam and transported upwards in the plume and significantly affected the plume dynamics. One-dimensional eruption column modelling suggests that the plume was dominated by steam, see Figure 2.1c taken from Mastin et al. (2024) and Wu et al. (2025). A plausible mechanism to form such a huge amount of water vapour involves a partially collapsing eruption plume that produces large-volume pyroclastic density currents. When these hot currents entered the ocean, they transferred their thermal energy to the water, which vaporised and rose buoyantly and vigorously in the upper atmosphere (Mastin et al., 2024; Wu et al., 2025). Sea salt on ash particles collected from the islands of Tonga further highlights the unusual composition of the plume and establishes the ocean, as opposed to the magma, as the source of the water vapour in the plume (Colombier et al., 2023).

2.2 Volcano-generated GW (and Lamb waves)

Due to its exceptional explosivity (Volcanic Explosivity Index (VEI) of 5.7; Poli and Shapiro, 2022), rapid development (less than a few hours), and the deep penetration of the plume up to the mesosphere, the climactic 15 January Hunga eruption triggered the generation of a broad spectrum of atmospheric waves. These include infrasound, Lamb waves, and stratospheric GW (Matoza et al., 2022; Vergoz et al., 2022; Wright et al., 2022). In the vertical, some of these waves were detected in every atmospheric layer from the surface to the edge of space, including from the mesosphere and lower thermosphere. These waves were either excited directly by the eruption or through multi-step vertical coupling and the generation of secondary wave modes (e.g., Vadas et al., 2023, see Chapter 6). The amplitudes of the wave trains from the Hunga eruption, as well as their propagation distances (several round-the-world journeys) are unprecedented in the satellite record.

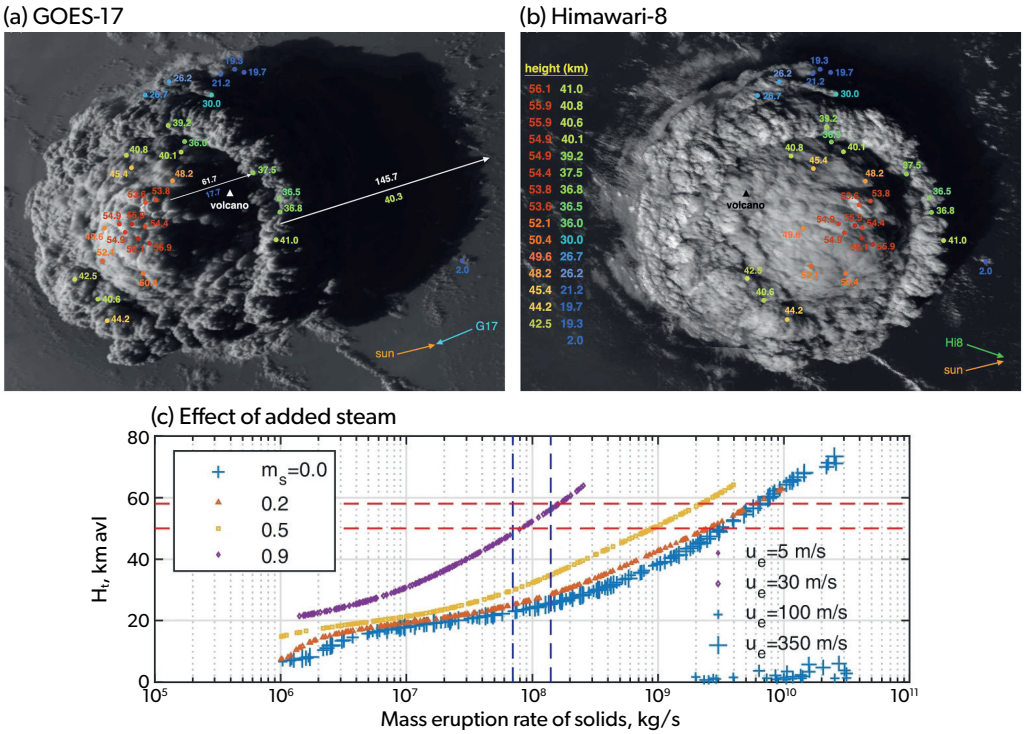

Figure 2.1: *Top row: Satellite images of the plume from (a) GOES-17 and (b) Himawari-8 on 15 January 2022 at 04:30 UTC. Coloured dots indicate stereo height estimates (in km), and the white/black triangles mark the position of the volcano. The white arrows in (a) indicate the shadow of a plume edge feature and a dome feature, with the shadow length above and the derived height below the arrow. The arrows in the lower right corners of the panels show the sun-to-pixel and satellite-to-pixel azimuths (taken from Carr et al., 2022). c) Relationship between plume top height and mass eruption rate (MER) of solids found by Monte-Carlo simulation using the 1-D volcanic plume rise model Plumeria. The different colours refer to the mass fraction of added steam (0, 0.2, 0.5, and 0.9). The red dashed lines indicate the range of plume top heights found in satellite observations. The blue dashed lines show the estimated range of the mass eruption rate derived from a comparison of fall deposit measurements with Ash3d simulations (taken from Mastin et al., 2024)*

2.2.1 Types of waves and early observations

The mesoscale patterns of atmospheric waves (excluding smaller-scale acoustic waves) can best be grasped by looking at successive maps of brightness temperature anomalies in the hours following the eruption, as shown in Figure 2.2a for the geostationary satellite Himawari (available at 10 min resolution). Concentric rings at the scale of the entire Pacific region can be clearly identified, corresponding to wave packets radiating away from the point-source volcano at different speeds. The image brings to mind the ripples that form on the surface of a pond after throwing a pebble into it, though at a very different scale. These rings have been observed in all terrestrial IR channels of geostationary satellite imagery, as well as dedicated imagers (Wright et al., 2022). According to their propagation speed, different wave types can be distinguished:

- First, Lamb wave pulses propagating at about 310 m/s. The Lamb wave is an external mode (edge wave), which can also be identified by its surface pressure signature. Global propagation of a Lamb wave was already documented from surface pressure observations after the eruption of Krakatau (VEI of 6) in 1883 (Symons et al., 1888). Fastest among the wave modes, the Lamb wave has the slowest decay time (Salby, 1979): after the Hunga eruption, the main Lamb wave pulse could be detected circling the globe at least four times (Matoza et al., 2022) and up to five times in satellite observations (Otsuka, 2022), i.e., travelling more than 100,000 km. It had a period of about 20–30 minutes (corresponding to a wavelength of about 500 km). The Lamb wave is weakly dispersive and the wave train propagation remains relatively isotropic for about half of the first transit to the antipodes, while variations in the wind, temperature and topography distort the phase lines for larger distances (Taylor, 1929; Garrett, 1969; Sepúlveda et al., 2023).

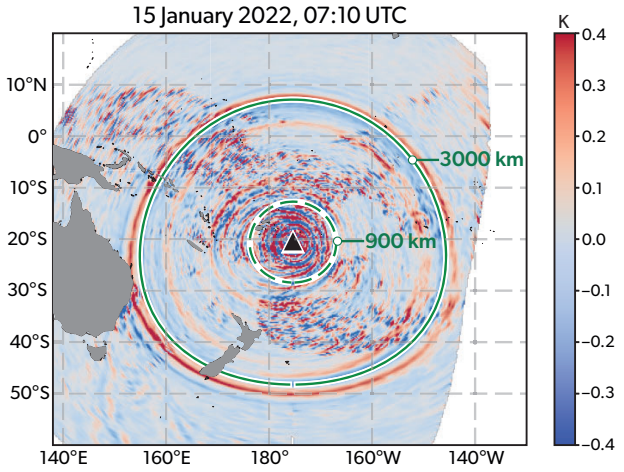

Figure 2.2: *Himawari brightness temperature second-order difference at 07:10 UTC on 15 January 2022 (channel 8), adapted after Matoza et al. (2022). Wave fronts associated with the leading Lamb wave and slower GW packets triggered by the eruption are clearly visible. Green circles are drawn to indicate equal distances from Hunga (dashed: 900 km; solid: 3,000 km).*

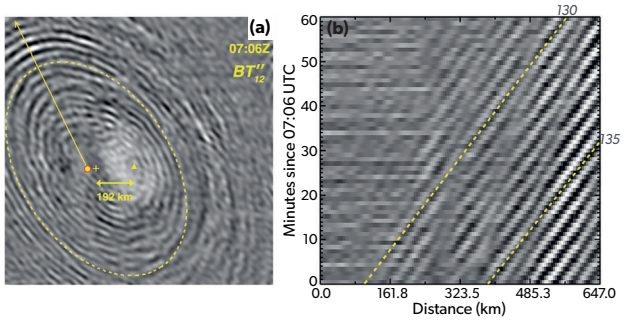

Figure 2.3: *Taken from Horváth et al. (2024), Figure 15. (a) Second-order derivative in time of the brightness temperature from GOES 17 channel 12 at 07:06 UTC filtered to emphasise the wave field and (b) time–distance plot for the period 07:06–08:06 UTC along the yellow arrow in panel (a). The interval used to calculate time derivatives is Δt = 1 min. The yellow dashed curve is an ellipse fitted to one of the concentric rings with its centre marked by the plus sign. The distance between the ellipse centre and Hunga (yellow triangle) is also indicated. The observed 192 km shift is due to advection of the wave field by the mean flow (see Horváth et al., 2024).*

- A train of slower GW with propagation speed up to 240 m/s. A noticeable feature in long-range propagation is the ~70 m/s gap in propagation speed between the Lamb wave and the fastest GW.

The leading GW packet, propagating at 240 m/s (i.e., Pekeris mode; Watanabe et al., 2022), was detected up to 10,000 km away from Hunga (Wright et al., 2022). Its decay is thus more than 10 times faster than that of the Lamb wave, in agreement with theoretical predictions (Salby, 1979). This mode is also more anisotropic than the Lamb wave, and its travel speed and dispersion depend on the propagation direction. While its signal is clearest in stratospheric temperatures, it has also been identified in surface pressure measurements (Watanabe et al., 2022).

The faster waves (Lamb wave and leading GW) are the only ones which were observed in the far field (>5,000 km away from the source). Other, slower GW are found closer to the volcano, but they cannot be traced further than 2,000 km away from Hunga. Dispersion is evident in those GW packets, with a slower and shorter-range propagation of the shorter horizontal wavelength waves. Due to their slower phase speed, shorter waves are more sensitive to the background wind, with dynamical processes such as Doppler shift or critical level filtering coming into play. Consistently, high-frequency (1 min) GOES brightness temperature imagery in the 9.6-micron band collected about three hours after the eruption reveal a rich small-scale wave field (Figure 2.2b): 50 m/s, ~5-minute period waves are observed. The distortion of the rings with a centre shifted West of Hunga is likely related to Doppler-shift by the background Westerlies (Horváth et al., 2024). Small to mesoscale GW persisted in the area of Hunga for more than 10 hours after the eruption peak, suggesting continuous generation during that period (e.g. Wright et al., 2022; Horváth et al., 2024).

2.2.2 Wave generation mechanisms, and what we can learn from the waves

The exact processes forcing the waves during the eruption and their relative importance are not entirely understood. Likely candidates include the explosions, volcanic jets and plume dynamics, as well as diabatic heating through heat exchange between the volcanic materials and surrounding air or latent heat release (i.e., through the condensation of steam water into ice). Despite remaining gaps in our understanding, gravity wave observations already provide key constraints on the eruption scenario. Precise records of the amplitude of the Lamb wave (5 hPa, 2,000 km away from the volcano) enabled estimations of the energy released by the eruption (Posey and Pierce, 1971; Matoza et al., 2022), at least relative to previous events, and showed it to be equivalent to the historical eruption of Krakatau in 1883. The waves also provide precious information on the eruption chronology, which can be most easily inferred from the

quasi-nondispersive Lamb wave. Back tracing the pressure maximum of the main Lamb pulse to the location of Hunga, it is possible to recover a time for the climax of the eruption (04:30 ± 5 min UTC, Wright et al., 2022) which falls within 5 minutes of the rising plume reaching its peak altitude (Carr et al., 2022). Besides the main Lamb waveform, earlier and later pulses of Lamb waves also bear the imprint of the complex eruption sequence, from its start between 04:00 and 04:15 UTC to a significant later explosion and plume around 08:40 UTC (Horváth et al., 2024). In general, notwithstanding time shifts related to the diversity of generation processes, there is a good correspondence between pulses of atmospheric waves and the plume dynamics inferred from geostationary satellites (Podglajen et al., 2022), or seismic activity (Vergoz et al., 2022). Further exploiting the waves to better constrain eruptive processes will require an interdisciplinary effort between volcanologists and atmospheric GW scientists.

2.3 Water vapour injection

A defining characteristic of the energetic underwater Hunga eruption was the amount of water vapour injected to high altitudes in the stratosphere (Table 2.2; Millán et al., 2022; Sellitto et al., 2022; Vömel et al., 2022; Khaykin et al., 2022; Randel et al., 2023). Steam (estimated to be more than 2900 Tg) likely accounted for 90% of the total injected material in mass (Van Eaton et al., 2023; Mastin et al., 2024; Wu et al., 2025).

During the climactic eruption on 15 January, the injection reached the mesosphere (~53 km), and water vapour saturated the stratospheric column up to about 35 km altitude within approximately one hour (Khaykin et al., 2022). Excess water condensed into hydrometeors (Vömel et al., 2022). Large anomalies in stratospheric water vapour concentrations of >7,000 ppmv up to 40 km altitude were recorded by GPS radio occultation (RO) measurements on the first day and of >1000 ppmv up to 30 km altitude by radiosonde measurements between days one and four (Figure 2.4; Vömel et al., 2022; Khaykin et al., 2022; Randel et al., 2023). The water vapour mixing ratio at ice saturation increased rapidly with altitude in the stratosphere, from approximately 10 ppmv at 17 km, to 100 ppmv at 21 km altitude, and to 1000 ppmv at 26 km (Vömel et al., 2022). The Aura Microwave Limb Sounder (MLS) retrievals of water vapour in the plume in the first four days are in agreement with these values, considering the coarse vertical resolution of the satellite retrievals (Millán et al., 2022). MLS

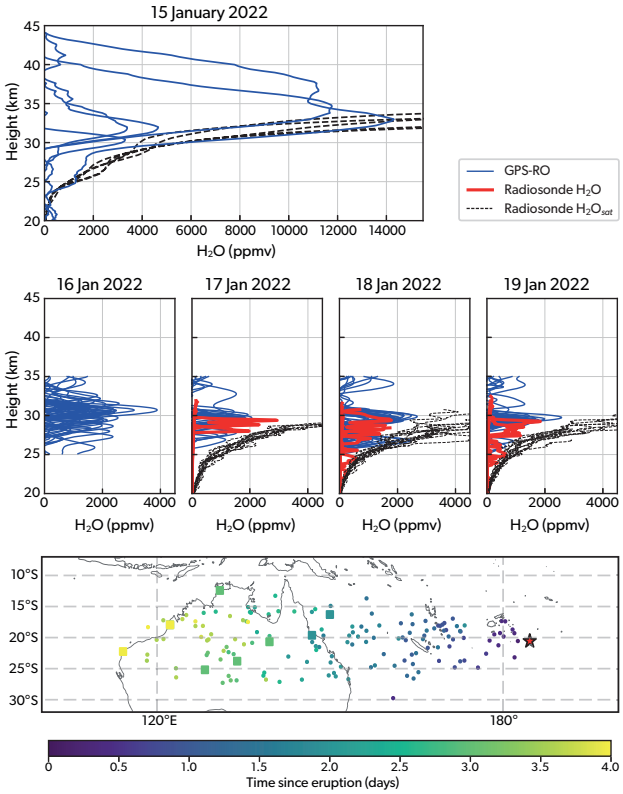

Figure 2.4: *(First two rows) Water vapour mixing ratio profiles (solid lines) in the Hunga plume, from GPS-RO and Australian radiosondes over January 15-19, 2022. Dashed lines are profiles of saturation mixing ratio. (Third row): Map of the soundings (GPS-RO as dots, radiosondes as squares; colour: time since main eruption). Data shown in Khaykin et al. (2022), Vömel et al. (2022) and Randel et al. (2023)*

first measured enhanced water vapour on 14 January near 18 km, injected by the 13–14 January smaller eruption (Millán et al., 2022).

The total water amount initially present in the plume is uncertain, but may have reached several thousands of Tg based on a 1-D steady plume model and observations of the umbrella growth-rate, the plume height, and the volume of tephra-fall deposits (Mastin et al., 2024; Wu et al., 2025). Most of it froze, and a fraction of the ice evaporated as it settled, thereby hydrating dry, stratospheric air at lower altitudes. The ice fallout likely contributed to the scavenging of ash and soluble gases, such as hydrogen chloride (HCl) (see Section 2.4 for details). The remaining 146 ± 5 Tg increased the global abundance of stratospheric water vapour by ~15%, representing an unprecedented jump in the observational record (see Figure 2.5a and Millán et al., 2022, for details). For comparison, the Calbuco eruption in 2015 reached an altitude of 21 km, directly injecting approximately

Table 2.2: *Injections from the eruption, including altitude, stratospheric injection amount, observing instruments (and simulations when applicable), and their publications.*

Volcanic aerosol/gas	Injection Altitude (km)	Stratospheric Injection (Gg)	Observing Instruments	Publication
H_2O (gas)	~27–35	146,000 ± 5,000	MLS	Millán et al. (2022)
			GPS-RO	Randel et al. (2023)
			RS41-RS	Vömel et al. (2022)
SO_2 (gas)	18–19 (13 Jan.)	60	OMPS, OMI, TROPOMI	Carn et al. (2022)
	>30 (15 Jan.)	400–480	MLS	Millán et al. (2022)
	Total Column	1000	EMI-2	Li et al. (2023)
			IASI	Legras et al. (2022)
				Sellitto et al. (2024)
HCl (gas)	20–25 (16–17 Jan.)	<1	MLS	Millán et al. (2022)
				Zhu et al. (2023)
BrO (gas)	8–15 (16–18 Jan.)	Negligible	EMI-2	Li et al. (2023)
				Zhu et al. (2023)
NO	~15–30	1.4–3.6*	GLD360	Zhu et al. (2023)
			WWLLN	
			ENTLN	
Primary solid aerosol (Ash or possibly sea salt)	>33–40	Likely small	AERONET	Boichu et al. (2023)
			Lidar	Baron et al. (2023)
			TROPOMI	
			Ash samples	Colombier et al. (2023)

*based on NO produced by each lightning flash from a global climate model

2 Tg water vapour into the lower stratosphere (Sioris et al., 2016). The MLS record shows numerous short-lived enhancements of approximately 10 ppmv below 20 km (at 68 hPa) following the Kasatochi eruption in 2008 and the Raikoke eruption in 2019, as well as the Calbuco eruption, due to the entrainment of water vapour from the troposphere into the stratosphere due to volcanic eruption columns (Glaze et al., 1997), and slightly larger, longer-lived enhancements following pyrocumulonimbus (see Figure 2.5a and Millán et al., 2022, for details). The hydration of the stratosphere on the scale of Hunga from a volcanic eruption had been proposed (Glaze et al., 1997), but never before observed. Typical volcanic eruptions reaching the stratosphere impact stratospheric water vapour, not through direct injection, but by increasing the tropical cold point temperatures and thereby increasing the entry of water vapour into the stratosphere as a result of aerosol radiative heating months after the eruption (Joshi and Shine, 2003).

Within two days of the eruption, the evaporation of sedimenting ice particles and strong horizontal and vertical wind shear, as may be expected during the SH summer circulation and Quasi-Biennial Oscillation (QBO) easterly phase, contributed to the appearance of thin slanted layers, with very high water vapour concentrations (see Figure 2.4a and Vömel et al., 2022, for details). The water vapour plume descended rapidly during the first two days after the eruption, at a rate of at least 1 km d^{-1}, due to a strong radiative cooling of the order of 10 K d^{-1} in potential temperature associated with the large water vapour enhancements, according to RO measurements (Randel et al., 2023). Thereafter, although still driven by radiative cooling, the descent rate slowed to approximately 0.2 km d^{-1}, with the water vapour enhancement observed above 29.5 km in January and below 26.5 km altitude by the first week of February (Sellitto et al., 2022; Legras et al., 2022). From the first week of February onward, the altitude of the water vapour plume levelled off (see Section 2.4 for details).

MLS shows water vapour anomalies of 1–2 ppmv persisting in the upper stratosphere between 35–50 km until the first week of February (Millán et al., 2022). Stratospheric water vapour concentrations in the plume decreased from <700 ppmv on the 19 January to <100 ppmv by mid-February as the plume spread,

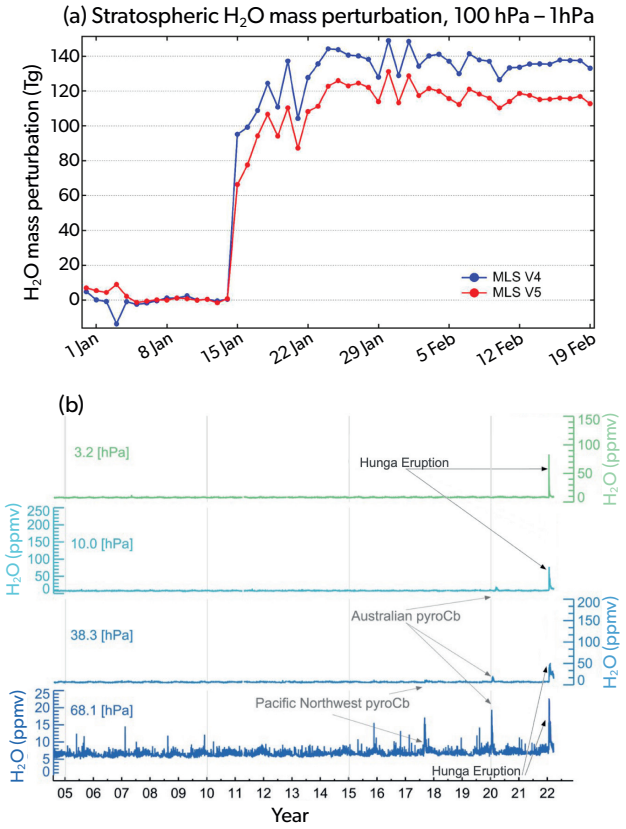

Figure 2.5: *a) Hunga-induced change in the total mass of stratospheric water vapour between 100–1 hPa pressure levels (16-50 km) using MLS V4 and MLS V5 data. Adapted from Khaykin et al. (2022). b) Time series of H_2O (MLS V4 data) mixing ratios at different pressure levels. Adapted from Millán et al. (2022).*

having circumnavigated the globe one and a half times (Vömel et al., 2022). MLS then showed the main water vapour plume had meridional (30°S–5°N) anomalies between 20–50 ppmv at altitudes between 17–26 km (Millán et al., 2022). Maximum water vapour concentrations were observed between 23–26.5 km by radiosondes, RO, and MLS (see Chapter 3 for a full discussion of the water vapour plume transport and dispersion after mid-February). A temperature pattern with negative temperature anomalies above the plume and positive temperature anomalies below the plume developed and lasted for weeks (Stocker et al., 2024), explained in part because water vapour effectively absorbs outgoing radiation (see Chapter 7 for details).

The large water vapour enhancements also accelerated the production of the hydroxyl radical (OH) in the plume above 25 km, likely doubling the availability of OH (Zhu et al., 2022) and hastening the conversion of sulfur dioxide (SO_2) to sulfate aerosol (see Section 2.5 for details). The change in OH concentration also led to rapid hydrogen oxide radicals (HO_x) cycling and the catalytic destruction of ozone (see Chapter 5 and Zhu et al., 2023, for details).

This large, quasi-instantaneous addition of water vapour to the stratosphere and the anomalies it produced in the first month remain exceptional in the observational record. Typical background stratospheric water vapour concentrations are 5 ppmv at 28 km, ranging from approximately 3 ppmv at the tropical tropopause to 7 ppmv in the upper stratosphere (Davis et al., 2016). The annual cycle in the lower stratosphere has an amplitude of approximately 3 ppmv amplitude. Observed trends in stratospheric water vapour from balloon-borne frost point measurements between 1980–2022 were largely positive ($\leq$1.2 ppmv decade^{-1} Hurst et al., 2011), but the anticipated increase in the tropical lower stratosphere related to greenhouse gas forcing is modest 0.31 ± 0.39 ppmv K^{-1} (Nowack et al., 2023). Removal of stratospheric water vapour occurs primarily through mean overturning Brewer-Dobson circulation, dehydration in the Antarctic polar vortex and Lyman-alpha photodissociation in the upper stratosphere, yielding an expected residence time of several years (see Chapter 7 for details). Enhancements in stratospheric water have radiative impacts (see Chapter 7), alter aerosol microphysical and radiative properties (see Section 2.6), and influence atmospheric chemistry (see Chapter 5) and atmospheric circulation (see Chapter 3).

2.4 Plume altitude and dispersion during the first month

Within the 10 hours following the initial eruption and after damping of the overshoot oscillations described in Section 2.1, GOES-17 observed the umbrella's descent, estimating a rate of approximately 1.7 km h^{-1} (Carr et al., 2022). Himawari-8 false color imagery confirmed the dissipation of the umbrella, which was attributed to the sedimentation of most large ice and ash particles (Legras et al., 2022).

The fast sedimentation of the condensed part of the volcanic plume, primarily composed of ice and ash, occurred within 15 hours of the eruption by 19:00 UTC on 15 January. The remaining plume led to multiple aerosol layers in the stratosphere from 18 km to >44 km. These layers were detected by multiple instruments in the following days. Two main clouds of aerosols, referred to as C1 and C2, emerged in the Himawari false colour imagery between 170°W and 177.5°W west of the maximum extent of the collapsing umbrella (Figure 2.6a–b; Carn et al., 2022;

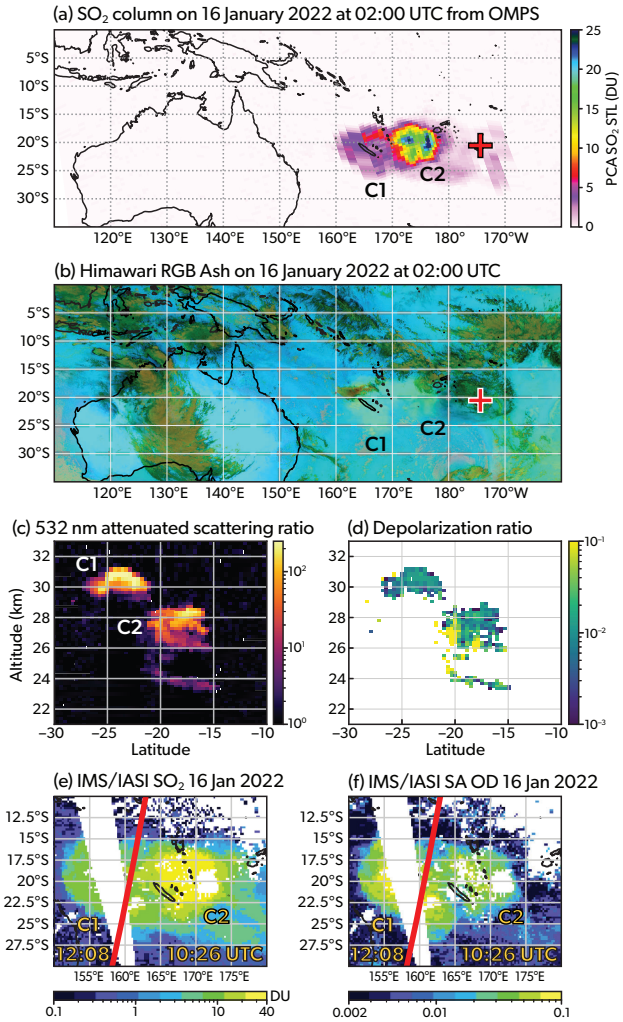

Figure 2.6: *a) SO_2 column for C1 and C2 clouds as seen from OMPS on 16 January 2022 at 2 UTC adapted from Carn et al. (2022) , b) Himawari false colour imagery using channels at 8.5, 10.4 and 12 µm for the same time showing C1 and C2 sulfate aerosols as greenish bright patches; brown patches are clouds and Australia is bright due its high infrared emission, c) 532 nm attenuated scattering ratio from CALIOP on 16 January 2022 at 15:08 UTC intersecting C1 and C2, d) depolarisation ratio in C1 and C2 at the same time, e) SO_2 column from IASI on 16 January 2026 from two swaths spanning C1 and C2, f) sulfate aerosol optical depth on the same swaths (mainly retrieved from 8.5 µm band). The red line in panels e) and f) is the CALIOP track shown in c) and d). b-f are adapted from Legras et al. (2022).*

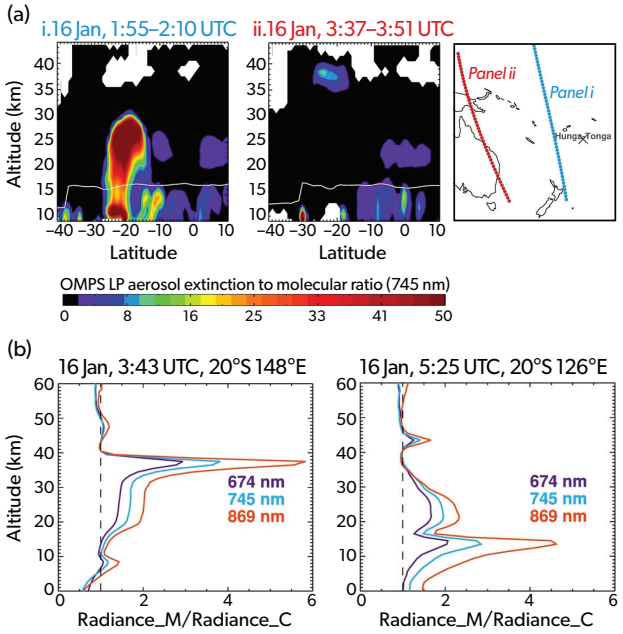

Figure 2.7: *(a) Plot of Ozone Monitoring and Profiler Suite aerosol extinction to molecular ratio profiles measured on 16 January 2022, 1 day after the main volcanic eruption. The right panel is the measurement's location. Blue is for the left panel, and red is for the centre. The white lines in the left and centre panels are the tropopause altitudes derived using the NASA Global modelling and Assimilation Office near-real time atmospheric analyses. (b) Plot of the measured to calculated radiance ratio (assuming aerosol-free atmosphere) profile for three wavelengths measured for two profiles taken on the same day. Taken from Taha et al. (2022).*

Legras et al., 2022). C1 and C2 were detected on 16 January by several instruments moving westward at about 20 m s^{-1}. At 2:45 UTC, the Cloud-Aerosol Lidar with Orthogonal Polarisation (CALIOP) showed C2 as an optically thick cloud, with a backscatter ratio at 532 nm larger than 200 between 26 and 29 km. Both of these clouds were mostly composed of poorly depolarising particles with small depolarising pockets (Sellitto et al., 2022; Legras et al., 2022; Boichu et al., 2023). Below this were optically thinner clouds at or below 20 km, with depolarising properties, which may partly be related to the eruption on 13 January (Zhu et al., 2022). Later at 15 UTC, CALIOP again identifies the C2 cloud between 26 and 28 km and the C1 cloud at 30–32 km with a stratospheric aerosol optical depth (AOD) greater than 0.5 (Figure 2.6c; Sellitto et al., 2022; Legras et al., 2022; Boichu et al., 2023). On the same day, the Ozone Mapping and Profiler Suite Limb Profiler (OMPS-LP), measured aerosols spread between 20–30 km and confirmed that aerosol from the first eruption on 13 January reached 20 km (Figure 2.7; Taha et al., 2022)

The depolarising pockets of the two main clouds were observed only over the first two days following the eruption, suggesting the presence of ice or ash. However, ice could not persist and UV instrument measurements show that absorbing aerosols dissipated in the days that followed, leaving the main volcanic plume composed primarily of SO_2 and rapidly forming sul-

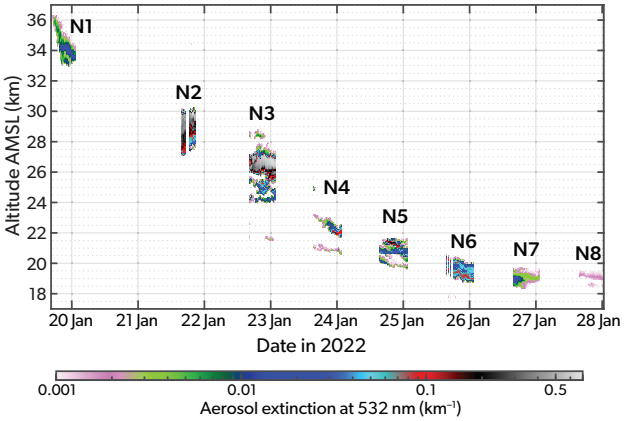

Figure 2.8: *Time-altitude curtain of aerosol extinction coefficient at 532 nm from 19-28 January. Layers are named N1 to N8, corresponding to every night of observations showing a significant aerosol burden. Taken from Baron et al. (2023).*

furic acid particles, hereafter referred to as sulfate aerosol (Sellitto et al., 2022; Taha et al., 2022; Legras et al., 2022). In the following days, the Multi-angle Imaging SpectroRadiometer (MISR) detected primarily spherical, non-absorbing particles, typical of volcanic sulfate aerosols in the stratosphere (Kahn et al., 2024). Ground-based Aerosol Robotic Network (AERONET) data was used to identify an unusual coarse mode that persisted during the first week of the plume's circumnavigation of the globe, attributed to sulfate-coated thin ash particles, though their altitude could not be determined (Boichu et al., 2023). Additionally, ground-based Lidar measurements at Réunion Island showed a negative or very small Ångström exponent on 21–22 January at altitudes of 22–29 km, indicating the presence of some relatively large aerosols (Figure 2.8; Baron et al., 2023). From the same location, Kloss et al. (2022) detected some partially absorbing particles near 22 km on 23 January and 20 km on 26 January.

The presence of ash and ice is not uncommon following volcanic eruptions (Rose et al., 1995; Brown et al., 2012; Romeo et al., 2025). However, the unusually large aerosol extinction and backscatter coefficients measured by OMPS-LP and CALIOP in the days after this eruption were surprising, particularly given the modest amounts of SO_2 injected into the stratosphere (see Section 2.1). The presence of large quantities of water vapour (see Section 2.3) led to an accelerated conversion to sulfate (see Section 2.5).

A smaller portion of the plume above 35 km (from the 15 January eruption), was detected by OMPS-LP (Figure 2.7; Taha et al., 2022) and by CALIOP as strongly depolarising particles on 15 January. This layer was detected where sulfate evaporates (Kremser et al., 2016), suggesting the presence of ultrafine ash (radius <1 μm). In fact, OMPS-LP measured aerosols between 40–50 km on the second day after the eruption and continued to measure the volcanic layer above 40 km for two weeks, and above 36 km for the following three months (Khaykin et al., 2022; Taha et al., 2022). Nonetheless, the aerosol loading above 35 km was minimal, and its relevance to climate and atmospheric chemistry is likely negligible.

Another secondary layer that formed at an altitude of 19–22 km moved slowly westward and possibly originated from a combination of the 13 January eruption plume and portions of the 15 January eruption plume, where the SO_2 separated from the water-rich plume at higher altitudes (Taha et al., 2022). As a result, the conversion from SO_2 to sulfates was much slower in that part of the plume than in the higher aerosol clouds. This layer was measured by the Portable Optical Particle Spectrometer (POPS) and SO_2 sondes over La Réunion on 24 and 25 January. These measurements showed that at altitudes of 19–22 km, where the air was drier, the effective radius of the particles was similar to background values of 0.2 μm (Asher et al., 2023); see also Section 2.6). On 25 January, simultaneous measurements of SO_2 and aerosols at 20 km revealed that SO_2 levels exceeded the H_2SO_4 aerosol mass, suggesting that the SO_2 oxidation rate was slower in this layer compared to the main layer, where water vapour was significantly elevated (Figure 2.11b; see also Section 2.5).

During the first two days after the eruption, the aerosol plume was confined in the 15°S–25°S band. Wind shear in the lower stratosphere, typical during the SH circulation and QBO easterly phase resulted in the appearance of a stretched aerosol layer at low altitudes within the first two weeks (Figure 2.8). In the following 10 days, while crossing the Indian Ocean, the plume rapidly dispersed in latitude to a domain extending from 30°S to 10°N (Figure 2.9; Taha et al., 2022; Schoeberl et al., 2023). The plume reached 10°N by 26 January, but then stopped this meridional expansion and remained essentially confined within this domain with a very slow expansion to 40°S–20°N over the following six months (Taha et al., 2022; Legras et al., 2022); see Chapter 3 for details. The same pattern was observed for water vapour (Khaykin et al., 2022).

The vertical motion of the aerosol plume was characterised by a fast initial descent of at least 400 m day^{-1}

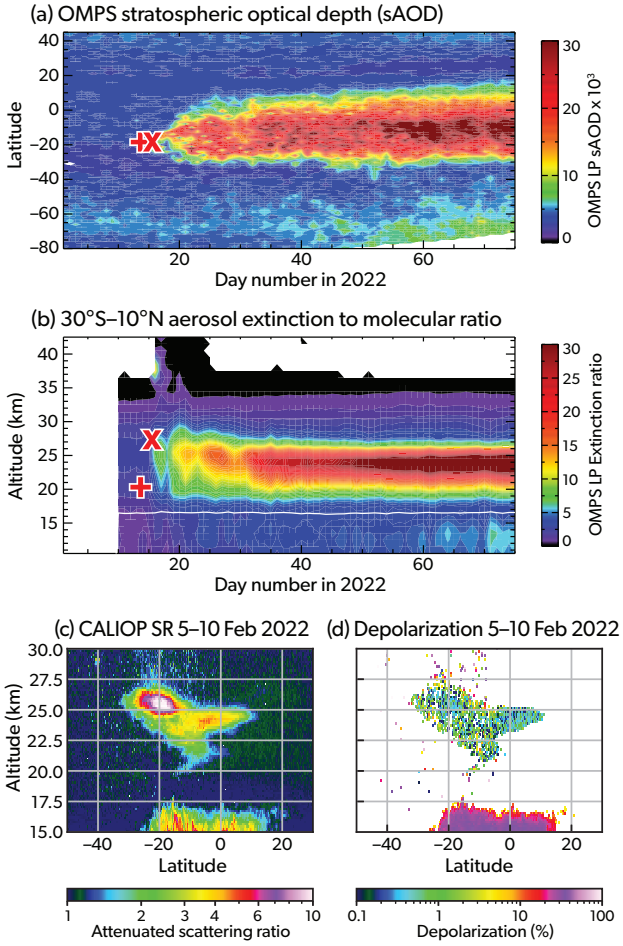

Figure 2.9: *(a) Plot of OMPS stratospheric optical depth (sAOD) x103 zonal mean at 869 nm for early 2022. (b) The extinction to molecular ratio zonal mean profiles between 30°S and 10°N for the same period. The white line is the tropopause altitude. The plus and cross and symbols in both figures are for the time and location of the two eruptions on 13 and 15 January (adapted from Taha et al., 2022). c-d) CALIOP mean scattering ratio and depolarisation averaged over all orbits during 5-10 February 2022. Below 17.5 km are tropical ice clouds (adapted from Legras et al., 2022).*

for the first 10 days within the moister parts of the sulfate layer (Sellitto et al., 2022). This descent corresponded to a cooling of 5 K day^{-1} in potential temperature, compatible with the initial water vapour descent reported in Section 2.3. Sellitto et al. (2022) attributed the descent to the radiative cooling by the water vapour infrared emission. Model simulations of the Hunga eruption also indicated that radiative cooling of water vapour was the primary driver of the rapid descent of the plume observed during the first two weeks of the eruption (Niemeier et al., 2023). After 27 January, the mean zonal MLS water vapour and CALIOP backscatter signals exhibit a descent pattern corresponding to a cooling of 4 K day^{-1} for another couple of weeks (Sellitto et al., 2022). Such intense and localised cooling is expected to induce a dynamical response (Podglajen et al., 2024), which in this case may have taken the form of an equatorial Rossby wave and led to the rapid transport across the equator on 20–23 January (Schoeberl et al., 2023).

After initially crossing the equator, zonal dispersion of the two main components of the plume was observed due to the westerly winds and the strong meridional shear that prevailed for several weeks at the latitude of the eruption and between 23 and 28 km altitude. As a result, the main plume completed its first circumnavigation of the globe in 15 days (Legras et al., 2022; Khaykin et al., 2022) and independent components merged rapidly and could not be distinguished by the beginning of February. Homogenisation of the main plume was slowed by the persistence of numerous compact anticyclonic patches of sulfate aerosols that might have been initially induced by the fast descent inside concentrated regions (Podglajen et al., 2024) and maintained afterwards by the ambient shear (Legras et al., 2022).

During the initial descent, the aerosols and the gas compounds (including water vapour and SO_2) remained well mixed (Sellitto et al., 2022). This phase ended by early February with the dilution of water vapour and the reduction of its radiative effect. Gravitational settling induced a slower but persisting descent of the aerosols (Asher et al., 2023) with respect to the ambient air, while the water vapour stalled and began an ascent due to the large-scale motion consistent with Brewer-Dobson circulation and the phase of the QBO (Schoeberl et al., 2023). As a result, the sulfate and the water plumes started to separate by mid-February at a rate of 16 m day^{-1} (Figure 2.10). Besides the direct impact on the plume altitude, the cooling effect of water persisted at a large scale and altered the circulation (Schoeberl et al., 2022; Coy et al., 2022).

2.5 Rapid formation of sulfate aerosol layer

Episodic volcanic eruptions remain one of the primary sources of SO_2 to the stratosphere (Robock, 2000; Kremser et al., 2016). On 16 January between approximately 23 and more than 33 km altitude, MLS detected SO_2 enhancements of >900 ppbv (Millán et al., 2022). Between 21 and 25 January and 18 and 30 km altitude, balloon instruments observed SO_2 enhancements >50 ppbv over Réunion Island (Figure 2.11a).

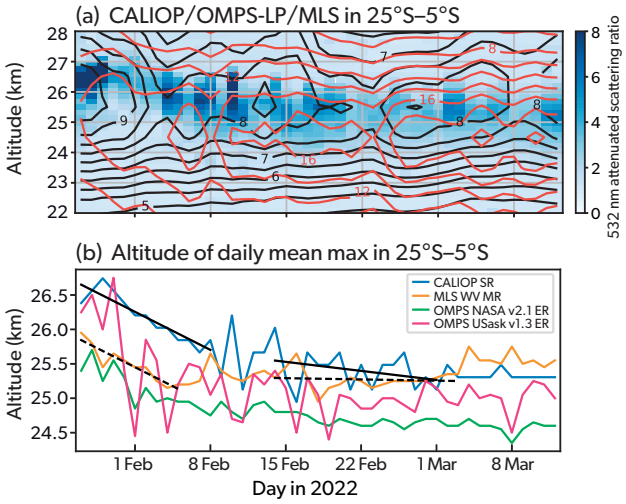

Figure 2.10: *. a) Comparative evolution of CALIOP attenuated scattering ratio (color), MLS water vapour mixing ratio (black contours, ppmv) , OMPS-LP 745 nm extinction ratio (red contours) based on the NASA v2.1 product as in Taha et al. (2022). b) daily mean vertical locations of maximum of aerosols ratios and water mixing ratio. All quantities are zonally averaged in the 25°S-5°S latitude band. Slopes are fitted for CALIOP scattering ratio and MLS water vapour: respectively -79.0 m d-1 and -78.8 m d-1 in the early period before 8 February and -18.8 m d-1 and -2.6 m d-1 in the second half of February. Both panels show common descent of water and aerosols until early February followed by vertical separation.*

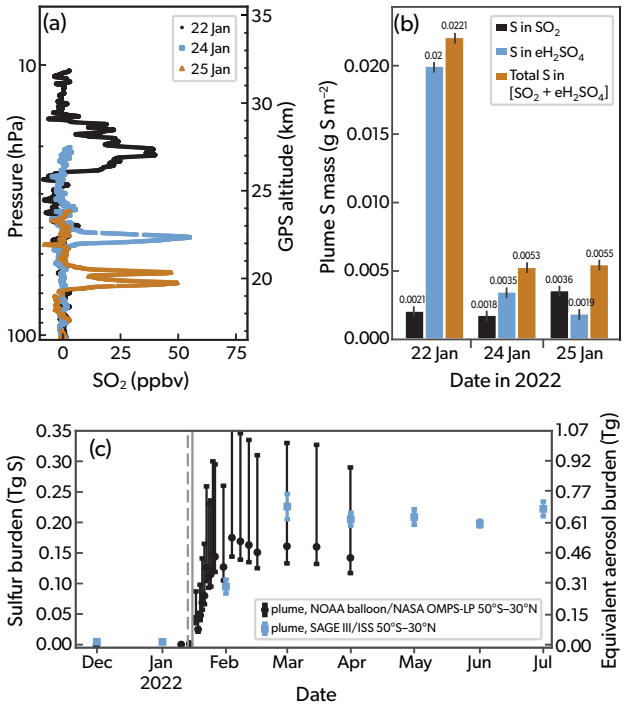

Figure 2.11: *Balloon-borne vertical profiles of SO_2 over the Maïdo in La Réunion. a) and b) adapted from Asher et al. (2023). c) The calculated total sulfur burden (and equivalent aerosol burden) calculated based on a combination of NASA OMPS-LP measurements and balloon-borne measurements, and from SAGE-III /ISS measurements assuming 70 percent weight of sulfuric acid in aerosol. Data in c) from Asher et al. (2023) and Duchamp et al. (2023). Error Bars represent the measurement uncertainty.*

As seen by Infrared Atmospheric Sounding Interferometer (IASI) (Figure 2.6e–f Legras et al., 2022; Sellitto et al., 2024), the conversion of SO_2 to sulfate aerosol was already underway in the C1 cloud at 10 UTC on 16 January due to the large injection of water vapour (see Section 2.3 for details), a few hours after the initial estimate of total SO_2 derived based on a Tropospheric Monitoring Instrument (TROPOMI) overpass at 2 UTC (Carn et al., 2022, see also Figure 2.6a). At this time, SO_2 was mostly concentrated in a horizontal patch corresponding roughly to C2 with no conversion yet to sulfates because of a drier environment. The analysis of subsequent evolution shows that no SO_2 is detected in C1 after 20 January (Legras et al., 2022). Carn et al. (2022) estimated a SO_2 e-folding time of $\tau = 6$ days based on satellite estimates of the SO_2 column and used this to estimate a total emitted mass of about 0.45 Tg of SO_2 from the 15 January eruption. This estimate was lately confirmed by Spurr et al. (2025). Including the contribution of the 13 January eruption (0.03 Tg sulfur or 0.06 Tg SO_2), the Carn et al. (2022) total estimate of sulfur injection is 0.25–0.27 Tg sulfur or 0.49–0.54 Tg SO_2 (Table 2.2). Other estimates from IASI are significantly higher at ~1 Tg SO_2 (Sellitto et al., 2022; Sellitto et al., 2024), a weather and climate model modelling study suggests 1.2 Tg (Bruckert et al., 2025), and one volcanology study proposes 1.3 Tg (Wu et al., 2025, and Table 2.2) (see discussion in Section 2.8). Estimates of the aerosol burden (~ 0.5 - 0.6 Tg) observed in subsequent weeks and months are consistent with the smaller 0.45 Tg SO2 injection (Asher et al., 2023; Duchamp et al., 2023). Estimated totals from the Hunga eruptions correspond to approximately 30% to 80% of the SO_2 emitted during the 2019 Raikoke eruption (1.5 Tg, Leeuw et al., 2021) and 2–5% of the SO_2 released during the 1991 Mt. Pinatubo eruption (20 Tg according to Bluth et al., 1992). Even the smallest estimate is more than double the amount of SO_2 needed to sustain the background stratospheric aerosol sulfur burden for one year (Feinberg et al., 2019).

CALIOP does not detect any significant depolarisation in C1 and C2, except marginally on their periphery on 16–17 January, possibly due to ice (Figure 2.6d). A significant depolarisation is only detected by

CALIOP on the low clouds seen on 16 January (Zhu et al., 2022) and on a high-altitude thin cloud between 34 and 39 km (see Section 2.4). At the same time, the UV instruments (Carn et al., 2022; Taha et al., 2022) do not detect any absorbing aerosol and MISR (Kahn et al., 2024) sees only spherical non-light-absorbing particles in C1 and C2. Ground-based photometric observations on 16 January (around 22:00 UTC) and following days also indicate an excess abundance of fine ($r_{\text{eff}} < 0.5\,\mu$m) poorly absorbing aerosols and also the presence of an unusual coarse mode (a few μm) possibly associated to sulfate coated ash (Boichu et al., 2023). depolarisation or light absorption were also occasionally observed in low clouds below 20 km (Kahn et al., 2024; Baron et al., 2023), possibly associated with the plume of the 13 January eruption. Besides these early features, no depolarisation or visible light absorption are detected by any spaceborne instrument during the subsequent evolution of the plume. We therefore conclude that almost all condensed material emitted during the eruption was scavenged by precipitations during the collapse of the umbrella clouds. As a consequence, it is more than likely that the aerosols were composed almost entirely of liquid sulfate droplets. The possible inclusion of solid nuclei inside these droplets cannot be ruled out but cannot be determined from remote sensing in the absence of optical signature.

On 20 January, the C1 and C2 clouds were located over the Indian ocean with a strong elongation in longitude from Australia to 60°E, due to the strong prevalent meridional shear at the altitudes of the clouds. IASI shows that on this date the conversion of the most western C1 to sulfate is achieved while the conversion of C2 is still in progress (Legras et al., 2022). A third cloud (C3) located to the north of C2, was identified drifting more slowly westward at a height of nearly 20 km and without a significant amount of sulfate aerosols. This cloud is a confirmation of the presence of drier layers in the initial distribution of SO_2 and of the heterogeneity of the plume.

Even if the clouds C1 and C2 were still spatially separated, it is likely that a significant amount of mixing had already occurred between them. The high moisture content implies radiative cooling and a mean descent of the clouds on the order of 350 m d^{-1} (12 K d^{-1} in potential temperature) from 27 January to 10 February, observed using mean aerosol scattering profiles retrieved from CALIOP (Sellitto et al., 2022). Large variation of this descent within the clouds is likely to have occurred according to the water vapour concentration.

As the plume passed over Réunion Island (21°S, 55°E) between 22 and 26 January, its components (the plume experienced significant wind shear as discussed above) passed in sequence from the highest and most humid to the lowest and driest (see Figure 2.8a; Kloss et al., 2022; Baron et al., 2023; Asher et al., 2023). in situ and ground based measurements confirmed the largest SO_2 conversion related to moisture (see Figure 2.11 and Asher et al., 2023), the low visible light absorption (Kloss et al., 2022; Boichu et al., 2023) and provided estimates of the size distribution with largest particles (r_{eff} about 0.4 μm, see Section 2.6 for more details) being consistently observed in the high plume (C1) (Baron et al., 2023; Asher et al., 2023; Boichu et al., 2023) and smaller values (0.2 μm) in the lowest part (C3). AERONET observations (Figure 2.12) document the rapid growth of Hunga aerosols from Australia to Réunion Island, with the column-integrated r_{eff} doubling in the first week after eruption (Boichu et al., 2023).

Mass estimate (based on OMPS-LP and balloon profiles) yields 0.18 Tg of sulfur in sulfate aerosol after 3 weeks (Asher et al., 2023) and stabilises after. This is in rough agreement with the stable estimate of 0.21 Tg found at later times between March and November 2022 (Duchamp et al., 2023) from NASA Stratospheric Aerosol and Gas Experiment onboard the international space station (SAGE III/ISS) and as mentioned above is compatible with the estimated initial injection (Carn et al., 2022).

Due to the large injection of water vapour, the conversion of SO_2 to sulfates, which usually occurs with an e-folding time of one month, occurred three times faster overall (Carn et al., 2022; Zhu et al., 2022; Asher et al., 2023), and SO_2 values returned to background levels by early February.

2.6 Microphysical and optical aerosol properties

The Hunga eruption produced a 4–5 fold global increase of the stratospheric aerosol optical depth (sAOD), according to OMPS-LP and SAGE III/ISS satellite observations (Taha et al., 2022; Khaykin et al., 2022). According to the Global Space-based Stratospheric Aerosol Climatology (GloSSAC), this perturbation represents the largest sAOD anomaly since the 1991 Mt. Pinatubo eruption, which was six times larger (Kovilakam et al., 2020). Total sAOD increased rapidly after the Hunga eruption (Kovilakam et al., 2020), reaching ~0.01 at 869 nm between 30°S and

15°N in less than two weeks according to OMPS-LP (Taha et al., 2022). Water vapour enhancements contributed minimally to ambient particle radius (< 10%) after one week (Asher et al., 2023).

As discussed in Section 2.5, the Hunga plume revealed its sheared plume structure. Between 17 January and mid-February, the aerosol size distribution was obtained from ground-based photometric observations at multiple stations of the worldwide AERONET network (Boichu et al., 2023) and from balloon-borne in situ measurements launched on several occasions over Réunion Island (Asher et al., 2023) (Figures 2.12 and 2.13). in situ balloon-borne measurements indicate that the main Hunga plume, defined as the part with the highest particle concentration, passed over Réunion Island above 25 km altitude between 22 January (parcel #0122 in Figure 2.12b) and 23 January (parcel #0123-a in Figure 2.12c), in agreement with ground-based Lidar observations (Figure 2.12f; Baron et al., 2023). During this first week, the number density in the plume was more than three times greater than in background air masses (Figure 2.13; Asher et al., 2023; Boichu et al., 2023). At that time, the volcanic parcels above 33 km were no longer observed (Taha et al., 2022; Baron et al., 2023). This main part of the plume (clouds C1 and C2) contained particles with $r_{\text{eff}} \geq 0.35\,\mu$m. A lower-altitude plume part (parcel #0123-b in Figure 2.12c below 25 km on 23 January) was populated by smaller particles with r_{eff} of 0.23 μm, a value comparable to the stratospheric baseline (~0.20 μm). On 22 January (11:41 UTC), AERONET recorded a column-integrated r_{eff} of 0.39 μm (Figure 2.13a). On the following days, Hunga aerosols from the plume tail were consistently detected at a much lower altitude, ~22 km on 24 January (Figure 2.12d) and ~20 km on 25 January (Asher et al., 2023), by balloon soundings and associated to lower r_{eff} of 0.19–0.20 μm, in agreement with AERONET observations (Figure 2.13a). According to AERONET observations on Réunion Island, a coarse mode with poorly-absorbing properties may have persisted from one to three weeks (Boichu et al., 2023). Submicron absorbing particles were also reported based on the Light Optical Aerosol Counter (LOAC) balloon soundings, measuring an absorption signal based on scattering from two angles, on 23 January at 23 km altitude and 26 January at 19 km altitude (Kloss et al., 2022).

After the first circumnavigation of the globe, an aerosol layer with a high effective radius (0.35–0.38 μm) was again detected over Réunion Island by AERONET (Figure 2.12a) and above 24 km by balloons

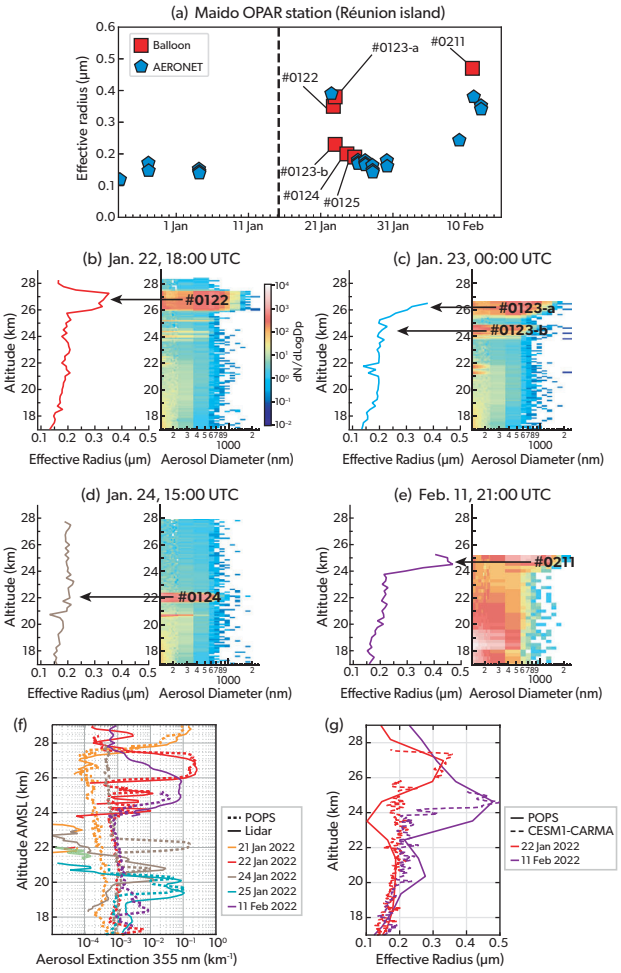

Figure 2.12: *Aerosol size over Maido OPAR station (Réunion Island) in the first month following eruption (until 15 February 2022). (a) Time series of effective radius (r_{eff} in µm) from balloon-borne measurements with POPS (maximum r_{eff}, as a function of altitude, within the Hunga plume) with red squares (from Asher et al., 2023) and from AERONET column-integrated effective radius with blue pentagons (Boichu et al., 2023). Plume parcels (#) are illustrated in panels b-e below. (b-e) Vertical distribution of effective radius (left) and aerosol number size distribution $dN/d\log D_p$ (right) up to an altitude of 30 km on (b) 22 Jan 18:00 UTC, (c) 23 Jan 00:00 UTC, (d) 24 Jan 15:00 UTC, (e) 11 Feb 21:30 UTC, b-e adapted from Asher et al. (2023). (f) Vertical profile of aerosol extinction at 355 nm calculated from POPS size distributions and Lidar backscatter observations (using vertical profiles of lidar ratios, i.e., aerosol extinction to backscatter coefficient ratios, derived from observations on each night). (g) Vertical distribution of aerosol effective radius on 22 January and 11 February from POPS observations (solid lines) and daily mean simulations with the CESM1-CARMA sectional aerosol model (dashed lines), adapted from Li et al. (2024).*

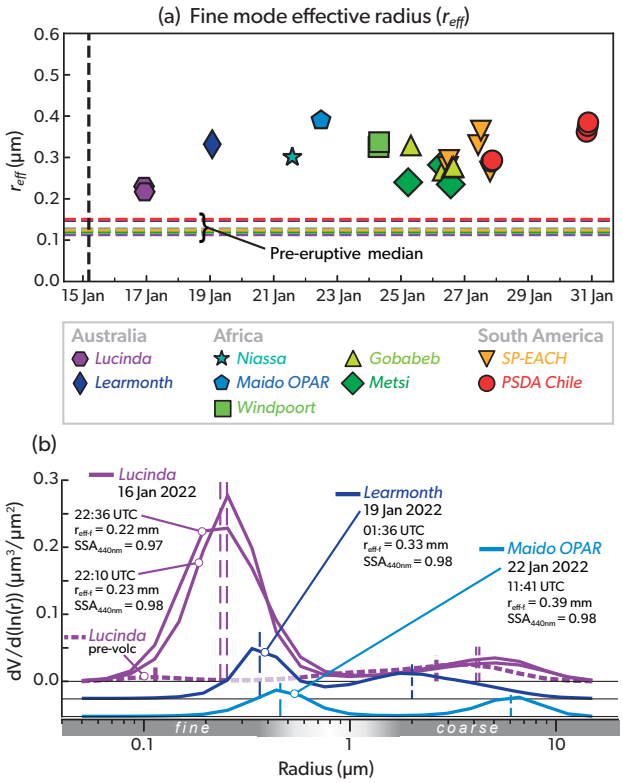

Figure 2.13: *(a) Time series of AERONET fine mode aerosol effective radius in January 2022 at 9 stations along the Hunga plume transport from Australia to South America (Lucinda and Learmonth in eastern/western Australia, Maïdo OPAR in Réunion Island, Niassa in Mozambique, Metsi in South Africa, Windpoort and Gobabeb in Namibia, SP-EACH in Brazil and PSDA Chile in Chile). Horizontal dashed lines indicate the median of fine mode radius values between 1 January 2020 and 15 January 2022 (date of the eruption) for each station. (b) Column-integrated aerosol volume size distribution and absorption properties (SSA_{440nm}) at Lucinda, Learmonth and Maïdo OPAR in the week after eruption, adapted from Boichu et al. (2023).*

on 11 February (Figure 2.12e), coexisting with large water vapour enhancements. Balloon observations show a higher aerosol effective radius on 11 February (0.47 µm) than on 22 January (0.35 µm) or 23 January (≥0.38 µm) (Figure 2.13); however, it is difficult to draw conclusions regarding the growth of particles based on so few in situ samples in a complex plume. On the other hand, AERONET measurements provide an average of the effective radius of aerosols across the atmospheric column that could be influenced by their vertical distribution.

Nevertheless, under the water-rich conditions of the plume, models replicate a similar increase in effective radius up to 0.35 µm in 3 weeks according to Zhu et al. (2022), and up to 0.5 µm by mid-February 2022 according to Li et al. (2024) (Figure 2.12g) due to accelerated SO_2 oxidation, particle nucleation, and heightened coagulation due to high particle number in the plume. Important differences between these studies include the use of a size-sectional aerosol model with a model vertical resolution of 3–4 km near 20 hPa (Li et al., 2024), compared to a modal aerosol model with a model vertical resolution of 1.5–2 km near 20 hPa (Zhu et al., 2022). Hunga particles grew much faster than Pinatubo particles, reaching a radius size of approximately 0.4 µm in one week instead of 4 months (Boichu et al., 2023). Particles from a number of recent eruptions (Kasatochi 2008, Sarychev 2009, Ambae 2018, Raikoke 2019, Ulawun 2019, La Soufrière 2022) did not grow this large (O'Neill et al., 2012; Jégou et al., 2013; Wrana et al., 2023; Boichu et al., 2023; Boone et al., 2024) (see Chapter 3) and stay basically under 0.2 µm.

Thereafter, the size stabilised near 0.4 µm for most of the plume (Khaykin et al., 2022; Asher et al., 2023; Boichu et al., 2023) and persisted over many months (Duchamp et al., 2023; Boichu et al., 2023, see Chapter 3 for details). The large aerosols of 0.4 µm in r_{eff} with narrow distribution (Duchamp et al., 2023) scatter incoming light very efficiently and so nearly maximise optical depth (Murphy et al., 2021). Therefore, despite the modest total mass of injected SO_2, particle sizes produced a relatively large radiative impact per unit mass of sulfate (Zhu et al., 2022).

2.7 Other plume chemical composition: minor injections of gas phase compounds and primary aerosols

2.7.1 Halogens

HCl and hydrogen bromide (HBr) are also emitted from volcanos. An HCl injection in the stratosphere was observed by Aura MLS at approximately 24 km altitude within one day of the eruption (Millán et al., 2022; Table 2.2). This small (likely less than 1 Gg; Zhu et al., 2023) injection, representing < 0.1% of organic chlorine in the stratosphere, resulted in elevated reactive chlorine, contributing to the rapid ozone depletion in the tropical stratosphere observed within one week of the eruption (see Evan et al., 2023, and Chapter 5 for details). Enhancements in reactive bromine (e.g., BrO), expected after rapid photolysis of HBr and/or other bromine reservoir Br species, were observed after the ~ 8 UTC eruption on 15 January between 8 and 15 km altitude, primarily in the troposphere (Li et al., 2023; Table 2.2). BrO emissions occurred after the SO_2 emissions, and <20% of the total BrO injection

was observed in the stratosphere, moving west, in the trailing edge of the SO_2 plume (Li et al., 2023). The Environmental Monitoring Instrument (EMI-2) could not provide information on the duration or the total BrO emission, but it is considered negligible (<0.001% of the inorganic bromine in the stratosphere), and did not appear to contribute to ozone depletion (Zhu et al., 2023). Differences in the altitudes of the SO_2, HCl and Br injections may be related to their solubility in water and scavenging by ice, or possibly the time at which they were released from the magmatic melt, although this topic remains an active area of research.

2.7.2 Lightning nitrogen oxide (NO)

The Hunga volcanic lightning (see Section 2.1) likely produced 1–4 Gg nitric oxide (NO) in situ at altitudes of 20–30 km based on reported lightning rates Zhu et al., 2023; see Chapter 5 for a discussion of its impact on stratospheric chemistry), exceeding previously reported rates in tropical storms and during other volcanic eruptions. For comparison, globally, lightning produces approximately 10 Tg yr^{-1} NO in the troposphere and occasionally overshoots the tropopause.

2.7.3 Ash and sea salt

A relatively small number of UV absorbing particles, indicative of ash, were observed in the high-altitude, leading edge of the plume as it travelled west (see Section 2.4 and Section 2.6 for details). Between 15–17 January, absorbing particles were observed over Eastern Australia between 35 and 40 km using a combination of CALIOP, Himawari-8, and OMPS-LP (e.g., Taha et al., 2022; Legras et al., 2022; Khaykin et al., 2022). Ground-based photometric measurements on 16 January also detected a slightly larger coarse mode over Eastern Australia, consistent with the presence of ash (Boichu et al., 2023). Lidar observations over Réunion Island on 19 January suggest the presence of absorbing particles in this leading edge of the plume (Baron et al., 2023). Based on extinction to backscatter ratios at a wavelength of 355 nm, up to 75% of this layer may have contained absorbing aerosols, such as fine ash. The AOD of this layer was ≤3.5% of that in the main part of the plume. A fraction (approximately 7% on average) of volcanic ash deposits, i.e., ~ 700 μm–2 mm diameter particles, collected from the islands of Tonga within two weeks of the eruption, also contained salts (e.g., NaCl, $CaSO_4$) bound to ash and other ions commonly found in seawater (e.g., Br, Mg, K; Colombier et al., 2023). The mass of sea salt in stratospheric particles is likely to be small compared to the gigantic amount of water vapour that remained in the stratosphere (see Zhu et al., 2023, and Section 2.3 for details), but remains an open question.

2.7.4 Ozone anomalies and the role of tropospheric transport

Anomalously low ozone was observed in the main, water-rich plume at altitudes between 26 and 30 km by balloons and MLS between 16–24 January (Evan et al., 2023; Zhu et al., 2023). The lowest ozone levels near Réunion Island were specifically observed by ozonesondes between 26 and 29 km on 21 and 22 January, with SO_2 interference accounting for approximately 3 to 4% of this decrease (Evan et al., 2023). MLS recorded the lowest O_3 levels at 27 km on 17 January near 20°S, east of Australia, on 20 January near 90°longitude, and on 24 January west of Africa (Zhu et al., 2023).

Climate model simulations, which consider both chemical and transport effects on the low ozone observed in the stratosphere after the eruption, suggest that a significant portion of this low ozone at 27 km (particularly from 15–18 January) may be attributed to the transport of low-ozone tropospheric air (Zhu et al., 2023). This contribution rapidly diminished from an estimated 50% on 16 January to approximately 10% on 22 January, primarily due to the short time required to produce ozone within the plume and the subsequent mixing and dilution of the injected air in the stratosphere (Zhu et al., 2023). Therefore, chemical processes, rather than tropospheric air transport, were the dominant factor in the observed ozone depletion after the initial injection phase (see Chapter 5 for details).

2.8 Sources of uncertainty

Several factors contribute to uncertainties in the initial injections of water, SO_2, ash and sea salt aerosol in the atmosphere, which remain an area of active research. Due to the nature of the energetic underwater eruption, empirical relationships between plume height and the mass eruption rate, used to calculate the emitted ashfall, do not apply (Mastin et al., 2024). Ocean-decolorisation suggests a minimum ashfall volume of 1.8 km^3 ± 0.4 km^3, which is approximately 12% of the caldera volume collapse (Kelly et al., 2024). Upper atmospheric composition observations are unavailable or unreliable within minutes of this eruption, and ground-based observations of tephra fall deposits landed primarily in the ocean, making it challenging to reconstruct their volume and dispersal

characteristics.

Especially during and in the first hours after the eruption, an optically thick plume, most likely consisting mainly of ash and ice made satellite measurements of the gas-phase composition difficult. The initial amount of injected ash and ice is itself very uncertain. The SO_2 burden estimated with four different UV satellite instruments immediately after the main eruption on 15 January was 0.5 Tg (Carn et al., 2022). Such measurements are well suited to measure the SO_2 burden. However, in estimates from infrared and microwave sounders the burden increased to about 1.0 Tg on 18 January, possibly due to the opacity of the early plume or instrumental saturation (Sellitto et al., 2022). Simulations using the ICOsahedral Nonhydrostatic model with Aerosols and Reactive Trace gases (ICON-ART), which is a weather and climate model, indicate that an initial injection of ~ 1.2 Tg of SO_2 is needed to reproduce observed SO_2 columns and sulfate sAOD (Bruckert et al., 2025). Similarly, sulfur degassing rates estimated from melt inclusions found in pyroclastic deposits are consistent with a larger SO_2 injection (1.3 Tg SO_2; Wu et al., 2025). Closure of the sulfur budget is not achieved given these higher estimations of SO_2 and the observed amount of sulfate aerosol (Asher et al., 2023; Duchamp et al., 2023). However, IASI is a total column measurement of SO_2, and uncertainties in the injection altitude of SO_2 in the stratosphere or in the troposphere could influence its atmospheric lifetime and its propensity to form sulfuric acid particles and grow to accumulation mode sizes that may be detected by balloons and space-based remote sensing instruments.

The amount of SO_2, HCl, HBr, and other halogens reaching the upper part of the plume strongly depends on their dissolution in water and scavenging by ice (e.g., Textor et al., 2003). The Hunga Volcano emitted large amounts of water vapour into the atmosphere, which was mostly converted to liquid water and ice (Van Eaton et al., 2023; Mastin et al., 2024). The role of liquid and solid hydrometeors in scavenging chemical compounds is an active area of research. However, the different injection heights for SO_2 and HCl (Millán et al., 2022) might be due to differences in the solubility in water and scavenging by ice and when compounds were released from the magmatic melt.

Space-borne and ground-based measurements consistently show that relatively few absorbing particles were observed beyond the first two days after the eruption (Taha et al., 2022; Legras et al., 2022; Baron et al., 2023). The presence of persisting ice instead of ash cannot be ruled out as these features rapidly vanish in the following days. These particles were primarily concentrated in the collapsing umbrella (Kahn et al., 2024), and then above 34 km in the leading edge of the plume. in situ balloon measurements of particle number and size and SO_2 in the plume within 7–10 days of the eruption are consistent with a short SO_2 lifetime and the rapid formation of a sulfate aerosol layer (below 30 km; Asher et al., 2023).

However, these measurements do not preclude the existence of sulfate-coated ash and/or sea salt particles within the plume. Additional balloon measurements within 11 days of the eruption suggested the presence of small absorbing particles below 23 km altitude (Kloss et al., 2022). These measurements should be interpreted with caution, however, due to the order of magnitude differences in calculated extinction based on these particle size distributions and simultaneous lidar measurements of extinction (Kloss et al., 2022). This is not the case for POPS measurements, which show good agreement with lidar measurements (see Section 2.6 for details).

A small but variable fraction of the ashfall contained salts and ions common in seawater (Colombier et al., 2023); see Sect 2.7.3 for details. Interestingly, little reactive chlorine (and no reactive bromine or iodine) is needed to explain the observed ozone depletion, and the eruption column was likely steam-driven, which would be poor in sea salt (see Zhu et al., 2023; Mastin et al., 2024, for details).

The inhomogeneity of the initial injection represents a final source of uncertainty because the kinetics of sulfate conversion and chemistry cannot be assumed uniform in the plume. In this respect, the modelling studies have been constrained to more or less arbitrary assumptions which differ from one study to the next. For instance, SO_2 and H_2O injections are not fully correlated in (Zhu et al., 2022) but they are in (Li et al., 2024).

The figures shown in this chapter are using version v2.1 of the OMPS-LP aerosol product like in Taha et al. (2022). It has been checked that using the new version v2.5 does not make a significant difference regarding the features discussed in this chapter.

2.9 The value of observations

The Hunga submarine volcano erupted in a very isolated and poorly monitored area at the surface in the South Pacific. Nevertheless, a tremendous amount of satellite and ground-based observations, in addition to opportunistic in situ measurements, were made

for this volcanic eruption. This is largely due to the number of satellite instruments which were operating at the time of the eruption and the large variety of their capabilities. Geostationary imagers GOES-17 and Himawari-8 covered the whole Southern Hemisphere equator at high frequency and were the first to witness the eruption, and proved particularly useful for determining the unprecedented altitude of the volcanic cloud and its subsequent collapse (Carr et al., 2022). The limb vertical profile measurements of MLS were crucial in showing the large amount of water vapour reaching the upper stratosphere and lower mesosphere (Millán et al., 2022), while a combination of the limb measurements of OMPS-LP and CALIOP Lidar provided an unprecedented view of the vertical and spatial distribution of the volcanic aerosol (Sellitto et al., 2022; Taha et al., 2022; Legras et al., 2022). Furthermore, multiple UV (TROPOMI, DSCOVR/EPIC, OMI, SNPP/OMPS and N20/NPP NM) and IR (IASI) nadir instruments tracked the volcanic plume as it circulated the globe, providing a fairly consistent estimate of the injected SO_2 and an early insight into the rapid SO_2 conversion to sulfate aerosol (Carn et al., 2022; Sellitto et al., 2022). These satellite observations were complemented by ground-based and in situ measurements from an international rapid response campaign on Réunion Island within one week of the eruption (Kloss et al., 2022; Baron et al., 2023; Asher et al., 2023; Evan et al., 2023) and by photometric observations from many AERONET ground stations of the Southern Hemisphere (Boichu et al., 2023). Furthermore, the Vaisala radiosonde (weather balloon) in situ measurements and RO, which are sufficiently sensitive to measure extreme water vapour amounts in the stratosphere, outside their standard operation range, were utilised to track the volcanic cloud, providing high-resolution vertical profiles of the stratospheric water vapour (Vömel et al., 2022; Khaykin et al., 2022). Within hours, information circulated and was exchanged on the Stratospheric sulfur and its Role in Climate (SSiRC) and volcanic group mailing lists, from which a fairly clear consensus on the eruption and its consequences emerged rapidly and was very helpful in the completion of the initial studies and their follow-up that led to this report.

References

Asher, E., M. Todt, K. Rosenlof, T. Thornberry, R.-S. Gao, G. Taha, P. Walter, S. Alvarez, J. Flynn, S. M. Davis et al. (2023). 'Unexpectedly rapid aerosol formation in the Hunga Tonga plume'. *Proc. Natl. Acad. Sci.*, 120, e2219547120. DOI: 10.1073/pnas.2219547120.

Astafyeva, E., B. Maletckii, T. D. Mikesell, E. Munaibari, M. Ravanelli, P. Coisson, F. Manta and L. Rolland (2022). 'The 15 January 2022 Hunga Tonga Eruption History as Inferred From Ionospheric Observations'. *Geophys. Res. Lett.*, 49, e2022GL098827. DOI: 10.1029/2022GL098827.

Baron, A., P. Chazette, S. Khaykin, G. Payen, N. Marquestaut, N. Bègue and V. Duflot (2023). 'Early Evolution of the Stratospheric Aerosol Plume Following the 2022 Hunga Tonga-Hunga Ha'apai Eruption: Lidar Observations From Reunion (21°S, 55°E)'. *Geophys. Res. Lett.*, 50, e2022GL101751. DOI: 10.1029/2022gl101751.

Bluth, G. J. S., S. D. Doiron, C. C. Schnetzler, A. J. Krueger and L. S. Walter (1992). 'Global tracking of the SO_2 clouds from the June, 1991 Mount Pinatubo eruptions'. *Geophys. Res. Lett.*, 19, pp. 151–154. DOI: 10.1029/91GL02792.

Boichu, M., R. Grandin, L. Blarel, B. Torres, Y. Derimian, P. Goloub, C. Brogniez, I. Chiapello, O. Dubovik, T. Mathurin et al. (2023). 'Growth and Global Persistence of Stratospheric Sulfate Aerosols From the 2022 Hunga Tonga–Hunga Ha'apai Volcanic Eruption'. *J. Geophys. Res.*, 128, e2023JD039010. DOI: 10.1029/2023JD039010.

Boone, C. D., P. F. Bernath, A. Pastorek and M. Lecours (2024). 'Sulfate aerosol properties derived from combining coincident ACE-FTS and SAGE III/ISS measurements'. *J. Quant. Spectrosc. Radiat. Transfer*, 312, 108815. DOI: 10.1016/j.jqsrt.2023.108815.

Bór, J., T. Bozóki, G. Sátori, E. Williams, S. A. Behnke, M. J. Rycroft, A. Buzás, H. G. Silva, M. Kubicki, R. Said et al. (2023). 'Responses of the AC/DC Global Electric Circuit to Volcanic Electrical Activity in the Hunga Tonga-Hunga Ha'apai Eruption on 15 January 2022'. *J. Geophys. Res.*, 128, e2022JD038238. DOI: 10.1029/2022JD038238.

Brown, R. J., C. Bonadonna and A. J. Durant (2012). 'A review of volcanic ash aggregation'. *Phys. Chem. Earth*, 45–46, pp. 65–78. DOI: 10.1016/j.pce.2011.11.001.

Bruckert, J., S. Chopra, R. Siddans, C. Wedler and G. A. Hoshyaripour (2025). 'Aerosol dynamic processes in the Hunga plume in January 2022: does water vapor accelerate aerosol aging?' *Atmos. Chem. Phys.*, 25, pp. 9859–9884. DOI: 10.5194/acp-25-9859-2025.

Carn, S. A., N. A. Krotkov, B. L. Fisher and C. Li (2022). 'Out of the blue: volcanic SO_2 emissions during the 2021-2022 Hunga Tonga-Hunga Ha'apai eruptions'. *Front. Earth Sci.*, 13. DOI: 10.3389/feart.2022.976962.

Carr, J. L., Á. Horváth, D. L. Wu and M. D. Friberg (2022). 'Stereo Plume Height and Motion Retrievals for the Record-Setting Hunga Tonga-Hunga Ha'apai Eruption of 15 January 2022'. *Geophys. Res. Lett.*, 49, e2022GL098131. DOI: 10.1029/2022gl098131.

Clare, M. A., I. A. Yeo, S. Watson, R. Wysoczanski, S. Seabrook, K. Mackay, J. E. Hunt, E. Lane, P. J. Talling, E. Pope et al. (2023). 'Fast and destructive density currents created by ocean-entering volcanic eruptions'. *Science*, 381, pp. 1085–1092. DOI: 10.1126/science.adi3038.

Colombier, M., I. A. Ukstins, S. Tegtmeier, B. Scheu, S. J. Cronin, S. Thivet, J. Paredes-Mariño, C. Cimarelli, K.-U. Hess, T. Kula et al. (2023). 'Atmosphere injection of sea salts during large explosive submarine volcanic eruptions'. *Sci. Rep.*, 13, 14435. DOI: 10.1038/s41598-023-41639-8.

Coy, L., P. Newman, K. Wargan, G. Partyka, S. Strahan and S. Pawson (2022). 'Stratospheric Circulation Changes Associated with the Hunga Tonga-Hunga Ha'apai Eruption'. *Geophys. Res. Lett.*, 49, e2022GL100982. DOI: 10.1029/2022GL100982.

Davis, S. M., K. H. Rosenlof, B. Hassler, D. F. Hurst, W. G. Read, H. Vömel, H. Selkirk, M. Fujiwara and R. Damadeo (2016). 'The Stratospheric Water and Ozone Satellite Homogenized (SWOOSH) database:a long-term database for climate studies'. *Earth Syst. Sci. Data*, 8, pp. 461–490. DOI: 10.5194/essd-8-461-2016.

Donner, S., A. Steinberg, J. Lehr, C. Pilger, P. Hupe, P. Gaebler, J. O. Ross, E. P. S. Eibl, S. Heimann, D. Rebscher et al. (2023). 'The January 2022 Hunga Volcano explosive eruption from the multitechnological perspective of CTBT monitoring'. *Geophys. J. Int.*, 235, pp. 48–73. DOI: 10.1093/gji/ggad204.

Duchamp, C., F. Wrana, B. Legras, P. Sellitto, R. Belhadji and C. von Savigny (2023). 'Observation of the aerosol plume from the 2022 Hunga Tonga–Hunga Ha'apai eruption with SAGE III/ISS'. *Geophys. Res. Lett.*, 50, e2023GL105076. DOI: 10.1029/2023GL105076.

Evan, S., J. Brioude, K. H. Rosenlof, R.-S. Gao, R. W. Portmann, Y. Zhu, R. Volkamer, C. F. Lee, J.-M. Metzger, K. Lamy et al. (2023). 'Rapid ozone depletion after humidification of the stratosphere by the Hunga Tonga eruption'. *Science*, 382, eadg2551. DOI: 10.1126/science.adg2551.

Feinberg, A., T. Sukhodolov, B.-P. Luo, E. Rozanov, L. H. E. Winkel, T. Peter and A. Stenke (2019). 'Improved tropospheric and stratospheric sulfur cycle in the aerosol–chemistry–climate model SOCOL-AERv2'. *Geosci. Model Dev.*, 12, pp. 3863–3887. DOI: 10.5194/gmd-12-3863-2019.

Garrett, C. J. R. (1969). 'Atmospheric edge waves'. *Q. J. R. Meteorol. Soc.*, 95, pp. 731–753. DOI: 10.1002/qj.49709540607.

Glaze, L. S., S. M. Baloga and L. Wilson (1997). 'Transport of atmospheric water vapor by volcanic eruption columns'. *J. Geophys. Res.*, 102, pp. 6099–6108. DOI: 10.1029/96JD03125.

Gupta, A. K., R. Bennartz, K. E. Fauria and T. Mittal (2022). 'Eruption chronology of the December 2021 to January 2022 Hunga Tonga-Hunga Ha'apai eruption sequence'. *Commun. Earth Environ.*, 3, 314. DOI: 10.1038/s43247-022-00606-3.

Horváth, Á., S. L. Vadas, C. C. Stephan and S. A. Buehler (2024). 'One-Minute Resolution GOES-R Observations of Lamb and Gravity Waves Triggered by the Hunga Tonga-Hunga Ha'apai Eruptions on 15 January 2022'. *J. Geophys. Res.*, 129, e2023JD039329. DOI: 10.1029/2023JD039329.

Hurst, D. F., S. J. Oltmans, H. Vömel, K. H. Rosenlof, S. M. Davis, E. A. Ray, E. G. Hall and A. F. Jordan (2011). 'Stratospheric water vapor trends over Boulder, Colorado: Analysis of the 30 year Boulder record'. *J. Geophys. Res.*, 116, D02306. DOI: 10.1029/2010JD015065.

Jarvis, P. A., T. G. Caldwell, C. Noble, Y. Ogawa and C. Vagasky (2024). 'Volcanic lightning reveals umbrella cloud dynamics of the 15 January 2022 Hunga volcano eruption, Tonga'. *B. Volcanol.*, 86, 54. DOI: 10.1007/s00445-024-01739-3.

Jégou, F., G. Berthet, C. Brogniez, J.-B. Renard, P. François, J. M. Haywood, A. Jones, Q. Bourgeois, T. Lurton, F. Auriol et al. (2013). 'Stratospheric aerosols from the Sarychev volcano eruption in the 2009 Arctic summer'. *Atmos. Chem. Phys.*, 13, pp. 6533–6552. DOI: 10.5194/acp-13-6533-2013.

Joshi, M. M. and K. P. Shine (2003). 'A GCM Study of Volcanic Eruptions as a Cause of Increased Stratospheric Water Vapor'. *J. Climate*, 16, pp. 3525–3534. DOI: 10.1175/1520-0442(2003)016<3525:AGSOVE>2.0.CO;2.

Kahn, R. A., J. A. Limbacher, K. T. Junghenn Noyes, V. J. B. Flower, L. M. Zamora and K. F. McKee (2024). 'Evolving Particles in the 2022 Hunga Tonga—Hunga Ha'apai Volcano Eruption Plume'. *J. Geophys. Res.*, 129, e2023JD039963. DOI: 10.1029/2023JD039963.

Kelly, L. J., K. E. Fauria, M. Manga, S. J. Cronin, F. H. Latu'ila, J. Paredes-Mariño, T. Mittal and R. Bennartz (2024). 'Airfall volume of the 15 January 2022 eruption of Hunga volcano estimated from ocean color changes'. *Bull. Volcanol.*, 86, 59. DOI: 10.1007/s00445-024-01744-6.

Khaykin, S., A. Podglajen, F. Ploeger, J.-U. Grooß, F. Tence, S. Bekki, K. Khlopenkov, K. Bedka, L. Rieger, A. Baron et al. (2022). 'Global perturbation of stratospheric water and aerosol burden by Hunga eruption'. *Commun. Earth Environ.*, 3, 316. DOI: 10.1038/s43247-022-00652-x.

Kloss, C., P. Sellitto, J.-B. Renard, A. Baron, N. Bègue, B. Legras, G. Berthet, E. Briaud, E. Carboni, C. Duchamp et al. (2022). 'Aerosol characterization of the stratospheric plume from the volcanic eruption at Hunga Tonga 15 January 2022'. *Geophys. Res. Lett.*, 49, e2022GL099394. DOI: 10.1029/2022GL099394.

Kovilakam, M., L. W. Thomason, N. Ernest, L. Rieger, A. Bourassa and L. Millán (2020). 'The Global Space-based Stratospheric Aerosol Climatology (version 2.0): 1979–2018'. *Earth Syst. Sci. Data*, 12, pp. 2607–2634. DOI: 10.5194/essd-12-2607-2020.

Kremser, S., L. W. Thomason, M. Von Hobe, M. Hermann, T. Deshler, C. Timmreck, M. Toohey, A. Stenke, J. P. Schwarz, R. Weigel et al. (2016). 'Stratospheric aerosol-Observations, processes, and impact on climate: Stratospheric Aerosol'. *Rev. Geophys.*, 54, pp. 278–335. DOI: 10.1002/2015RG000511.

Leeuw, J. de, A. Schmidt, C. S. Witham, N. Theys, I. A. Taylor, R. G. Grainger, R. J. Pope, J. Haywood, M. Osborne and N. I. Kristiansen (2021). 'The 2019 Raikoke volcanic eruption – Part 1: Dispersion model simulations and satellite retrievals of volcanic sulfur dioxide'. *Atmos. Chem. Phys.*, 21, pp. 10851–10879. DOI: 10.5194/acp-21-10851-2021.

Legras, B. (2025). 'Hunga eruption on 15 January 2022: was there a precursor plume one hour before the eruption?' EarthArXiV manuscript. DOI: 10.31223/X5DT8F.

Legras, B., C. Duchamp, P. Sellitto, A. Podglajen, E. Carboni, R. Siddans, J.-U. Grooß, S. Khaykin and F. Ploeger (2022). 'The evolution and dynamics of the Hunga Tonga–Hunga Ha'apai sulfate aerosol plume in the stratosphere'. *Atmos. Chem. Phys.*, 22, pp. 14957–14970. DOI: 10.5194/acp-22-14957-2022.

Li, C., Y. Peng, E. Asher, A. A. Baron, M. Todt, T. D. Thornberry, S. Evan, J. Brioude, P. Smale, R. Querel et al. (2024). 'Microphysical Simulation of the 2022 Hunga Volcano Eruption Using a Sectional Aerosol Model'. *Geophys. Res. Lett.*, 51, e2024GL108522. DOI: 10.1029/2024GL108522.

Li, Q., Y. Qian, Y. Luo, L. Cao, H. Zhou, T. Yang, F. Si and W. Liu (2023). 'Diffusion Height and Order of Sulfur Dioxide and Bromine Monoxide Plumes from the Hunga Tonga–Hunga Ha'apai Volcanic Eruption'. *Remote Sens.*, 15, 1534. DOI: 10.3390/rs15061534.

Mastin, L. G., A. R. Van Eaton and S. J. Cronin (2024). 'Did steam boost the height and growth rate of the giant Hunga eruption plume?' *Bull. Volcanol.*, 86, 64. DOI: 10.1007/s00445-024-01749-1.

Matoza, R. S., D. Fee, J. D. Assink, A. M. Iezzi, D. N. Green, K. Kim, L. Toney, T. Lecocq, S. Krishnamoorthy, J.-M. Lalande et al. (2022). 'Atmospheric waves and global seismoacoustic observations of the January 2022 Hunga eruption, Tonga'. *Science*, 377, pp. 95–100. DOI: 10.1126/science.abo7063.

Millán, L., M. L. Santee, A. Lambert, N. J. Livesey, F. Werner, M. J. Schwartz, H. C. Pumphrey, G. L. Manney, Y. Wang, H. Su et al. (2022). 'The Hunga Tonga-Hunga Ha'apai Hydration of the Stratosphere'. *Geophys. Res. Lett.*, 49, e2022GL099381. DOI: 10.1029/2022gl099381.

Murphy, D. M., K. D. Froyd, I. Bourgeois, C. A. Brock, A. Kupc, J. Peischl, G. P. Schill, C. R. Thompson, C. J. Williamson and P. Yu (2021). 'Radiative and chemical implications of the size and composition of aerosol particles in the existing or modified global stratosphere'. *Atmos. Chem. Phys.*, 21, pp. 8915–8932. DOI: 10.5194/acp-21-8915-2021.

Niemeier, U., S. Wallis, C. Timmreck, T. van Pham and C. von Savigny (2023). 'How the Hunga Tonga—Hunga Ha'apai Water Vapor Cloud Impacts Its Transport Through the Stratosphere: Dynamical and Radiative Effects'. *Geophys. Res. Lett.*, 50, e2023GL106482. DOI: 10.1029/2023gl106482.

Nowack, P., P. Ceppi, S. M. Davis, G. Chiodo, W. Ball, M. A. Diallo, B. Hassler, Y. Jia, J. Keeble and M. Joshi (2023). 'Response of stratospheric water vapour to warming constrained by satellite observations'. *Nat. Geosci.*, 16, pp. 577–583. DOI: 10.1038/s41561-023-01183-6.

O'Neill, N. T., C. Perro, A. Saha, G. Lesins, T. J. Duck, E. W. Eloranta, G. J. Nott, A. Hoffman, M. L. Karumudi, C. Ritter et al. (2012). 'Properties of Sarychev sulphate aerosols over the Arctic'. *J. Geophys. Res.*, 117, 2011JD016838. DOI: 10.1029/2011JD016838.

Otsuka, S. (2022). 'Visualizing Lamb Waves From a Volcanic Eruption Using Meteorological Satellite Himawari-8'. *Geophys. Res. Lett.*, 49, e2022GL098324. DOI: 10.1029/2022GL098324.

Podglajen, A., A. Le Pichon, R. F. Garcia, S. Gérier, C. Millet, K. Bedka, K. Khlopenkov, S. Khaykin and A. Hertzog (2022). 'Stratospheric Balloon Observations of Infrasound Waves From the 15 January 2022 Hunga Eruption, Tonga'. *Geophys. Res. Lett.*, 49, e2022GL100833. DOI: 10.1029/2022GL100833.

Podglajen, A., B. Legras, G. Lapeyre, R. Plougonven, V. Zeitlin, V. Brémaud and P. Sellitto (2024). 'Dynamics of diabatically forced anticyclonic plumes in the stratosphere'. *Q. J. R. Meteorol. Soc.*, 150, pp. 1538–1565. DOI: 10.1002/qj.4658.

Poli, P. and N. M. Shapiro (2022). 'Rapid Characterization of Large Volcanic Eruptions: Measuring the Impulse of the Hunga Tonga Ha'apai Explosion From Teleseismic Waves'. *Geophys. Res. Lett.*, 49, e2022GL098123. DOI: 10.1029/2022GL098123.

Posey, J. W. and A. D. Pierce (1971). 'Estimation of Nuclear Explosion Energies from Microbarograph Records'. *Nature*, 232, pp. 253–253. DOI: 10.1038/232253a0.

Prata, F., A. T. Prata, R. Tanner, R. G. Grainger, M. Borgas and T. J. Aubry (2025). 'The radial spreading of volcanic umbrella clouds deduced from satellite measurements'. *Volcanica*, 8, pp. 1–29. DOI: 10.30909/vol.08.01.0129.

Proud, S. R., A. T. Prata and S. Schmauß (2022). 'The January 2022 eruption of Hunga Tonga-Hunga Ha'apai volcano reached the mesosphere'. *Science*, 378, pp. 554–557. DOI: 10.1126/science.abo4076.

Purkis, S. J., S. N. Ward, N. M. Fitzpatrick, J. B. Garvin, D. Slayback, S. J. Cronin, M. Palaseanu-Lovejoy and A. Dempsey (2023). 'The 2022 Hunga-Tonga megatsunami: Near-field simulation of a once-in-a-century event'. *Sci. Adv.*, 9, eadf5493. DOI: 10.1126/sciadv.adf5493.

Randel, W. J., B. R. Johnston, J. J. Braun, S. Sokolovskiy, H. Vömel, A. Podglajen and B. Legras

(2023). 'Stratospheric Water Vapor from the Hunga Tonga–Hunga Ha'apai Volcanic Eruption Deduced from COSMIC-2 Radio Occultation'. *Remote Sens.*, 15, 2167, p. 2167. DOI: 10.3390/rs15082167.

Robock, A. (2000). 'Volcanic eruptions and climate'. *Rev. Geophys.*, 38, pp. 191–219. DOI: 10.1029/1998RG000054.

Romeo, F., L. Mereu and S. Scollo (2025). 'Ash and Ice Aggregation in Satellite Retrieval: The 15 January 2022 Hunga Tonga-Hunga Ha'apai Hydromagmatic Eruption'. *J. Geophys. Res.*, 130, e2024JD041196. DOI: 10.1029/2024JD041196.

Rose, W. I., D. J. Delene, D. J. Schneider, G. J. S. Bluth, A. J. Krueger, I. Sprod, C. McKee, H. L. Davies and G. G. J. Ernst (1995). 'Ice in the 1994 Rabaul eruption cloud: implications for volcano hazard and atmospheric effects'. *Nature*, 375, pp. 477–479. DOI: 10.1038/375477a0.

Salby, M. L. (1979). 'On the Solution of the Homogeneous Vertical Structure Problem for Long-Period Oscillations'. *J. Atmos. Sci.*, 36, pp. 2350–2359. DOI: 10.1175/1520-0469(1979)036<2350:OTSOTH>2.0.CO;2.

Schoeberl, M. R., Y. Wang, R. Ueyama, G. Taha, E. Jensen and W. Yu (2022). 'Analysis and Impact of the Hunga Tonga-Hunga Ha'apai Stratospheric Water Vapor Plume'. *Geophys. Res. Lett.*, 49, e2022GL100248. DOI: 10.1029/2022gl100248.

Schoeberl, M. R., Y. Wang, R. Ueyama, G. Taha and W. Yu (2023). 'The Cross Equatorial Transport of the Hunga Tonga-Hunga Ha'apai Eruption Plume'. *Geophys. Res. Lett.*, 50, e2022GL102443. DOI: 10.1029/2022gl102443.

Seabrook, S., K. Mackay, S. J. Watson, M. A. Clare, J. E. Hunt, I. A. Yeo, E. M. Lane, M. R. Clark, R. Wysoczanski, A. A. Rowden et al. (2023). 'Volcaniclastic density currents explain widespread and diverse seafloor impacts of the 2022 Hunga Volcano eruption'. *Nat. Commun.*, 14, 7881. DOI: 10.1038/s41467-023-43607-2.

Sellitto, P., A. Podglajen, R. Belhadji, M. Boichu, E. Carboni, J. Cuesta, C. Duchamp, C. Kloss, R. Siddans, N. Bègue et al. (2022). 'The unexpected radiative impact of the Hunga Tonga eruption of 15th January 2022'. *Commun. Earth Environ.*, 3, 288. DOI: 10.1038/s43247-022-00618-z.

Sellitto, P., R. Siddans, R. Belhadji, E. Carboni, B. Legras, A. Podglajen and et al. (2024). 'Observing the SO_2 and sulfate aerosol plumes from the 2022 Hunga eruption with the Infrared Atmospheric Sounding Interferometer (IASI)'. *Geophys. Res. Lett.*, 51, e2023GL105565. DOI: 10.1029/2023GL105565.

Sepúlveda, I., M. Carvajal and D. C. Agnew (2023). 'Global Winds Shape Planetary-Scale Lamb Waves'. *Geophys. Res. Lett.*, 50, e2023GL106097. DOI: 10.1029/2023GL106097.

Sioris, C. E., A. Malo, C. A. McLinden and R. D'Amours (2016). 'Direct injection of water vapor into the stratosphere by volcanic eruptions'. *Geophys. Res. Lett.*, 43, pp. 7694–7700. DOI: 10.1002/2016GL069918.

Spurr, R. J. D., M. Christi, N. A. Krotkov, W.-E. Choi, S. Carn, C. Li, N. Kramarova, D. Haffner, E.-S. Yang, N. Gorkavyi et al. (2025). 'Solar Backscatter Ultraviolet (BUV) Retrievals of Mid-Stratospheric Aerosols from the 2022 Hunga Eruption'. *EGUsphere [preprint]*, 2025, pp. 1–43. DOI: 10.5194/egusphere-2025-2938.

Stocker, M., A. K. Steiner, F. Ladstädter, U. Foelsche and W. J. Randel (2024). 'Strong persistent cooling of the stratosphere after the Hunga eruption'. *Commun. Earth Environ.*, 5, 450. DOI: 10.1038/s43247-024-01620-3.

Symons, G. J. et al., eds. (1888). *The Eruption of Krakatoa and Subsequent Phenomena: report of the Krakatoa committee of the Royal Society*. UK: Trübner & Company, p. 494.

Taha, G., R. Loughman, P. R. Colarco, T. Zhu, L. W. Thomason and G. Jaross (2022). 'Tracking the 2022 Hunga Tonga-Hunga Ha'apai Aerosol Cloud in the Upper and Middle Stratosphere Using Space-Based Observations'. *Geophys. Res. Lett.*, 49, e2022GL100091. DOI: 10.1029/2022gl100091.

Taylor, G. I. (1929). 'Waves and tides in the atmosphere'. *Proc. R. Soc. Lond. A*, 126, pp. 169–183. DOI: 10.1098/rspa.1929.0213.

Textor, C., H.-F. Graf, M. Herzog and J. M. Oberhuber (2003). 'Injection of gases into the stratosphere by explosive volcanic eruptions'. *J. Geophys. Res.*, 108, 2002JD002987. DOI: 10.1029/2002JD002987.

Vadas, S. L., E. Becker, C. Figueiredo, K. Bossert, B. J. Harding and L. C. Gasque (2023). 'Primary and secondary gravity waves and large-scale wind changes generated by the Tonga volcanic eruption on 15 January 2022: Modeling and comparison with ICON-MIGHTI winds'. *J. Geophys. Res.*, 128, e2022JA031138. DOI: 10.1029/2022JA031138.

Van Eaton, A. R., J. Lapierre, S. A. Behnke, C. Vagasky, C. J. Schultz, M. Pavolonis, K. Bedka and K. Khlopenkov (2023). 'Lightning Rings and Gravity Waves: Insights Into the Giant Eruption Plume

From Tonga's Hunga Volcano on 15 January 2022'. *Geophys. Res. Lett.*, 50, e2022GL102341. DOI: 10.1029/2022gl102341.

Vergoz, J., P. Hupe, C. Listowski, A. Le Pichon, M. A. Garcés, E. Marchetti, P. Labazuy, L. Ceranna, C. Pilger, P. Gaebler et al. (2022). 'IMS observations of infrasound and acoustic-gravity waves produced by the January 2022 volcanic eruption of Hunga, Tonga: A global analysis'. *Earth Planet. Sci. Lett.*, 591, 117639. DOI: 10.1016/j.epsl.2022.117639.

Vömel, H., S. Evan and M. Tully (2022). 'Water vapor injection into the Stratosphere by Hunga Tonga-Hunga Ha'apai'. *Science*, 377, pp. 1444–1447. DOI: 10.1126/science.abq2299.

Watanabe, S., K. Hamilton, T. Sakazaki and M. Nakano (2022). 'First Detection of the Pekeris Internal Global Atmospheric Resonance: Evidence from the 2022 Tonga Eruption and from Global Reanalysis Data'. *J. Atmos. Sci.*, 79, pp. 3027–3043. DOI: 10.1175/JAS-D-22-0078.1.

Wrana, F., U. Niemeier, L. W. Thomason, S. Wallis and C. Von Savigny (2023). 'Stratospheric aerosol size reduction after volcanic eruptions'. *Atmos. Chem. Phys.*, 23, pp. 9725–9743. DOI: 10.5194/acp-23-9725-2023.

Wright, C. J., N. P. Hindley, M. J. Alexander, M. Barlow, L. Hoffmann, C. N. Mitchell, F. Prata, M. Bouillon, J. Carstens, C. Clerbaux et al. (2022). 'Surface-to-space atmospheric waves from Hunga Tonga-Hunga Ha'apai eruption'. *Nature*, 609, pp. 741–746. DOI: 10.1038/s41586-022-05012-5.

Wu, J., S. J. Cronin, M. Brenna, S.-H. Park, A. Pontesilli, I. A. Ukstins, D. Adams, J. Paredes-Mariño, K. Hamilton, M. Huebsch et al. (2025). 'Low sulfur emissions from 2022 Hunga eruption due to seawater–magma interactions'. *Nat. Geosci.*, 18, pp. 518–524. DOI: 10.1038/s41561-025-01691-7.

Zhu, Y., C. G. Bardeen, S. Tilmes, M. J. Mills, X. Wang, V. L. Harvey, G. Taha, D. Kinnison, R. W. Portmann, P. Yu et al. (2022). 'Perturbations in stratospheric aerosol evolution due to the water-rich plume of the 2022 Hunga-Tonga eruption'. *Commun. Earth Environ.*, 3, 248. DOI: 10.1038/s43247-022-00580-w.

Zhu, Y., R. W. Portmann, D. Kinnison, O. B. Toon, L. Millán, J. Zhang, H. Vömel, S. Tilmes, C. G. Bardeen, X. Wang et al. (2023). 'Stratospheric ozone depletion inside the volcanic plume shortly after the 2022 Hunga Tonga eruption'. *Atmos. Chem. Phys.*, 23, pp. 13355–13367. DOI: 10.5194/acp-23-13355-2023.